THE ASTROPHYSICAL JOURNAL, 551:461–477, 2001 April 10

EARLY DUST EVOLUTION IN PROTOSTELLAR ACCRETION DISKS

GERHARD SUTTNER AND HAROLD W. YORKE
Astronomisches Institut der Universität Würzburg, Am Hubland, 97074 Würzburg, Germany; and Jet Propulsion Laboratory, California Institute of Technology, MS 169-506, 4800 Oak Grove Drive, Pasadena, CA 91109; suttner@astro.uni-wuerzburg.de, Harold.Yorke@jpl.nasa.gov
Received 2000 April 24; accepted 2000 December 12

ABSTRACT

We investigate dust dynamics and evolution during the formation of a protostellar accretion disk around intermediate-mass stars via two-dimensional numerical simulations. Using three different detailed dust models, compact spherical particles, fractal ballistic particle cluster agglomeration (BPCA) grains, and ballistic cluster cluster agglomeration (BCCA) grains, we find that even during the early collapse and the first $\sim 10^4$ yr of dynamical disk evolution, the initial dust size distribution is strongly modified. Close to the disk's midplane coagulation produces dust particles of sizes of several times 10 μm (for compact spherical grains) up to several millimeters (for fluffy BCCA grains), whereas in the vicinity of the accretion shock front (located several density scale heights above the disk), large velocity differences inhibit coagulation. Dust particles larger than about 1 μm segregate from the smaller grains behind the accretion shock. Because of the combined effects of coagulation and grain segregation, the infrared dust emission is modified. Throughout the accretion disk a Mathis, Rumpl, & Nordsieck dust distribution provides a poor description of the general dust properties. Estimates of the consequences of the "freezing out" of molecules in protostellar disks should consider strongly modified grains. Physical model parameters such as the limiting sticking strength and the grains' resistivity against shattering are crucial factors determining the degree of coagulation reached. In dense regions (e.g., in the midplane of the disk) a steady state is quickly attained; for the parameters used here the coagulation timescale for 0.1 μm dust particles is ~ 1 yr (10^{-12} g cm$^{-3}/\varrho$). High above the equatorial plane coagulation equilibrium is not reached as a result of the much lower densities. Here the dust size distribution is affected primarily by differential advection, rather than coagulation. The influence of grain evolution and grain dynamics on the disk's near-infrared continuum appearance during the disk's formation phase is only slight because the most strongly coagulated grains are embedded deep within the accretion disk.

Subject headings: accretion, accretion disks — hydrodynamics — radiative transfer — solar system: formation — stars: formation

1. INTRODUCTION

Dust in protostellar envelopes and accretion disks is a major component of prestellar matter, strongly influencing the thermodynamical and gasdynamical behavior of these young objects as well as their observable appearance. Dust provides the seeds for planetesimals, which in turn evolve into the constituents of a planetary system: comets, planets, moons, and the debris associated with asteroids and Kuiper belt objects. Interstellar dust evolves significantly from its initial state in recently formed molecular clouds up to the formation of planetesimals around stars, and as the gas density increases, it does so at an ever increasing rate. In molecular clouds it takes several times 10^6 yr to build up large fluffy grains by dust coagulation (Ossenkopf 1993; Weidenschilling & Ruzmaikina 1994). In the midplane of accretion disks this timescale shrinks to about 10^2 yr as a result of the high densities there (Mizuno, Markiewicz, & Völk 1988; Mizuno 1989; Schmitt, Henning, & Mucha 1997).

It would be naive to imply, however, that it is only a matter of time before coagulation produces the first planetesimals of several kilometers in size. Other processes affect grain growth and evolution: orbital decay, shattering, cratering, sputtering, and compacting of amorphous grains, in addition to adsorption, outgassing, and chemical reprocessing of molecules. These processes depend critically on the physical conditions within the disk and on the grains' relative velocities. Large compact dust grains ($\gtrsim 10$ μm) can decouple from the gas and gain large relative velocities to each other that could prevent coagulation due to a limited sticking strength. By contrast, large fractal dust grains, such as ballistic cluster cluster agglomeration (BCCA) particles, are always well coupled to the gas component; large BCCA particles do not achieve sufficient relative velocities to coagulate effectively (Schmitt et al. 1997). The assumption of an "intermediate" type of fractal grains, the so-called ballistic particle cluster agglomeration (BPCA) particles, could alleviate this problem. Such coagulates possibly couple sufficiently well to the gas to prevent high relative velocities and behave in the limit of a large number of constituent grains like compact particles, so that turbulence and systematic relative velocities can drive coagulation (Ossenkopf 1993).

A high sticking strength is a necessary prerequisite for effective coagulation up to planetesimal sizes, since turbulent relative velocities can prevent the coagulation of preplanetesimal dust grains (Weidenschilling & Cuzzi 1993). This could be achieved with ice or frost layers on the colliding particles' surfaces (Bridges et al. 1996; Supulver et al. 1997).

Dust coagulation leads to important modifications of the protostellar matter. Turbulence in accretion disks is strongly coupled to the opacity of the medium, which in turn is dependent on the type of dust material and the dust grain size distribution. A high degree of coagulation implies significant reduction of the dust opacity (Mizuno et al. 1988). Reduced opacity is necessary to damp turbulence that otherwise would be a major obstacle for the preplanetesimal dust particles to settle down to the disk's equa-

torial plane (Weidenschilling 1984). During the formation of an accretion disk, however, virtually unprocessed dust material is continuously being supplied by the parent molecular cloud core. "Second generation" coagulation occurs (Mizuno 1989), which also influences opacity and the dynamics of the disk.

For this study we calculated the dust evolution during the formation of a protostellar accretion disk using a multicomponent radiation hydrodynamics (RHD) code, an improved version of an RHD code designed for one component (Yorke, Bodenheimer, & Laughlin 1995; Yorke & Bodenheimer 1999). Different dust models are applied, and the influence of the dust-dust sticking strength is investigated. Brownian motion, turbulence, differential radiative acceleration, and gravitative sedimentation with size-dependent relaxation timescales are considered as sources of relative velocities between the dust grains. Mean dust opacities are calculated directly from the actual dust size distribution and are continuously updated in the radiation transport module. Finally, a diagnostic frequency and angle-dependent radiation transport code are used to produce synthetic dust continuum emission maps and spectra that give information on observational consequences.

In § 2 we describe our models for the dust, and in § 3 we sketch our numerical approach to the problem. The initial conditions for the particular cases considered are introduced in § 4, and the numerical results of the simulations are presented in § 5. Finally, in § 6 these results are discussed in light of observable consequences, and conclusions are drawn.

2. PHYSICS OF DUST GRAINS IN STAR-FORMING REGIONS

According to our present picture of the interstellar medium, dust grains more or less uniformly permeate gas clouds, contributing about 1% of their total mass. The grain size distribution follows a power law with an exponent of about -3.5 (Mathis, Rumpl, & Nordsieck 1977, hereafter MRN77). MRN77 estimated maximum and minimum grain sizes at several nanometers and several microns, respectively. The constituent dust grains were assumed to be mainly "astrophysical" silicates with some contribution by "graphites." With this dust model they could fit the overall extinction curve of the diffuse interstellar medium quite well. However, observations of dense molecular cloud cores show that the upper limiting grain size is shifted to larger radii (polarization measurements of Vrba, Coyne, & Tapia 1993; theoretical predictions by Fischer, Henning, & Yorke 1994). Coagulation is assumed to grow large grains in this environment.

Three different dust models are considered. First, we treat the dust as compact spherical particles. For this model there are several theoretical studies that deal with dust opacities (Yorke 1988), sticking strengths (Chokshi, Tielens, & Hollenbach 1993), the physics of dust shattering (Jones, Tielens, & Hollenbach 1996), and gas-dust coupling strengths (Yorke 1979). Thus, the basic physical properties are reasonably well defined, although more recent experimental work indicates that the critical sticking velocities tend to be higher than theoretical estimates by about a factor of 10 (Poppe & Blum 1997).

We next consider fractal BPCA grains and BCCA grains. Ossenkopf (1993) developed a theoretical dust model for these fluffy particles and provided analytical expressions for the gas-dust and the dust-dust interaction cross sections as a function of the compact volume of the grains. Henning & Stognienko (1996) have calculated opacities for these fractal dust particles, and Wurm (1997) generalized the sticking strength of Chokshi et al. (1993) to fractal coagulates. Again, recent experimental studies indicate critical sticking velocities to be about an order of magnitude larger than the theoretical values (Poppe & Blum 1997).

2.1. *Compact Spherical Grains*

2.1.1. *Opacities and Radiative Acceleration*

Because dust is the predominant source of extinction in the temperature, density, and wavelength regimes considered (e.g., Yorke & Henning 1994), we have included only the dust's contribution to opacity and radiative acceleration. The specific extinction $\kappa_{\lambda,i}^{\rm ext}$ of the component i at wavelength λ is proportional to the specific cross section of the spherical grains:

$$\kappa_{\lambda,i}^{\rm ext} = \frac{Q_{\lambda,i}^{\rm ext}\,\pi a_i^2}{m_i}\,, \tag{1}$$

$$\kappa_{\lambda}^{\rm ext} = \frac{\sum_{i=1}^{N} \varrho_i \kappa_{\lambda,i}^{\rm ext}}{\sum_{i=1}^{N} \varrho_i}\,, \tag{2}$$

$$\kappa_{\lambda,i}^{p} = \kappa_{\lambda,i}^{\rm ext}(1 - A_{\lambda,i}\, g_{\lambda,i})\,. \tag{3}$$

The extinction gain factor $Q_{\lambda,i}^{\rm ext}$, the albedo $A_{\lambda,i}$, and the asymmetry parameter $g_{\lambda,i} = \langle \cos \Theta_\lambda \rangle_i$ are calculated from Mie theory using the dielectric constants for "astronomical" silicates given by Draine & Lee (1984). The net specific extinction of the dust grains $\kappa_\lambda^{\rm ext}$ is the weighted sum over the different constituent grain sizes (Fig. 1). Here $\kappa_{\lambda,i}^{p}$ is the specific radiation pressure opacity needed to determine the interaction of the dust particles with the stellar radiation flux $\boldsymbol{F}_\lambda$. The radiative acceleration of the dust particles is given by

$$\left(\frac{\partial \boldsymbol{v}_i}{\partial t}\right)_{\rm rad} = \frac{1}{c}\int_0^\infty \kappa_{\lambda,i}^{p}\,\boldsymbol{F}_\lambda\, d\lambda\,. \tag{4}$$

2.1.2. *Sticking of Grains*

Sticking of the spherical dust grains can be described by application of the theory of elasticity (Chokshi et al. 1993).

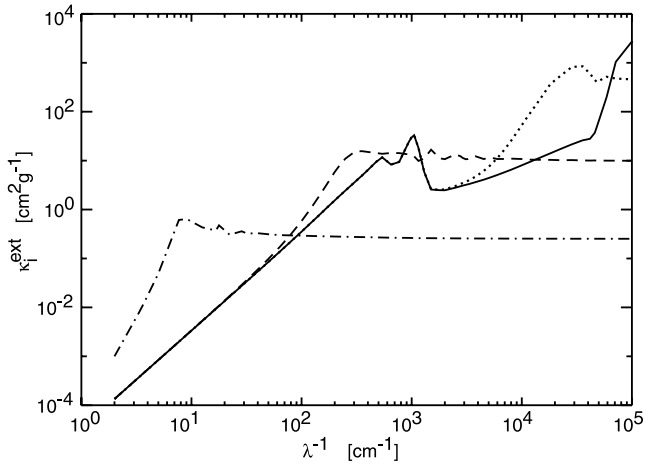

FIG. 1.—Specific extinction coefficient of compact spherical dust grains with sizes of 5 nm (*solid line*), 0.1 μm (*dotted line*), 5 μm (*dashed line*), and 0.2 mm (*dot-dashed line*).

One determines the binding energy of two spheres brought together under consideration of elastic wave dissipation in the two bodies. The resultant binding energy is set equal to the relative kinetic energy of the two colliding particles. This gives a critical sticking velocity, above which coagulation ceases and the particles bounce. Thus, $v_{\rm stick}$ is given by

$$E_{\rm stick} = 9.6\gamma^{5/3}R^{4/3}E^{-2/3}\,, \tag{5}$$

$$v_{\rm stick} = \sqrt{\frac{2E_{\rm stick}}{\mu}}\,. \tag{6}$$

The constants γ and E denote the surface energy per unit area and Young's modulus of the dust material, respectively. $R = r_1 r_2/(r_1 + r_2)$ is the reduced radius of the contact surfaces, and $\mu = m_1 m_2/(m_1 + m_2)$ is the reduced mass of the two colliding dust particles. This expression differs by a numerical factor of about 3 from the original formula by Chokshi et al. (1993) when applied to spheres because a correction of Dominik & Tielens (1997) has been applied (see discussion by Wurm 1997). Note that Beckwith, Henning, & Nakagawa (2000) give a slightly different formula for $v_{\rm stick}$ (quoting the same authors as above):

$$v_{\rm stick} = 1.07\,\frac{\gamma^{5/6}}{R^{5/6}E^{1/3}\rho_g^{1/2}}\,, \tag{7}$$

where ρ_g is the specific mass of the grain material. Equations (5) and (6) and equation (7) are identical when $r_1 = r_2$ and $m_1 = m_2$ but differ by 18% (50%) when the mass ratio of the colliding particles is 10 (100) and by a factor of almost 2 for extreme dust mass ratios.

An ice layer on the grains' surfaces enhances the critical sticking velocity by more than an order of magnitude compared to a pure silicate surface. The ice surfaces are destroyed at dust temperatures of about 125 K. Thus, pure silicate grains are assumed where the dust temperature exceeds the ice melting limit. According to the experiments of Poppe & Blum (1997), the critical sticking velocities are increased by a factor of 10 for the simulations.

2.1.3. *Grain Shattering*

When the relative velocity rises above a critical velocity $v_{\rm crit}$, the dust particles are shattered. This is a gradual process, starting with crater formation on the grains' surfaces and ending with total disruption of projectile and target. We assume a critical shattering velocity $v_{\rm crit}$ for silicates (see Jones et al. 1996):

$$v_{\rm crit} = 2.7\ {\rm km\ s^{-1}}\,.$$

Jones et al. (1996) also give analytic expressions for the ejected mass during a shattering encounter. When half of the mass of the target particle (the larger of two colliding dust grains) is shocked, they assume total disruption; the debris particles are assumed to follow a power-law size distribution with an exponent of -3.0 to -3.5. In our simulations we choose an exponent of -3.5. The upper size limit of the fragments first grows with increasing collision velocity (i.e., increasing crater volume) and starts to decrease inversely proportional to the relative velocity when disruption starts (see the Appendix).

2.1.4. *Gas-Dust Interaction*

The dust grains are coupled to the gas by dynamical friction. According to the gas densities in star-forming regions, the Epstein coupling law (Epstein 1923; Weidenschilling 1977) is valid because the mean free path λ_f of the gas molecules is large compared to the radii of the dust particles:

$$\lambda_f = \frac{1}{n_{\rm gas}\sigma_{\rm gas}} \approx 10^5\ {\rm cm}\left(\frac{\varrho}{10^{-14}\ {\rm g\ cm^{-3}}}\right)^{-1} \gg a_i\,. \tag{8}$$

Here we use an extension of the Epstein law for superthermal relative velocities (Yorke 1979), which often occur in later stages of the protostellar collapse:

$$\left(\frac{\partial \boldsymbol{v}_i}{\partial t}\right)_{\rm ww} = \frac{4}{3}\,\varrho\,\frac{\sigma_i}{m_i}\,\sqrt{c_s^2 + (\boldsymbol{v} - \boldsymbol{v}_i)^2}(\boldsymbol{v} - \boldsymbol{v}_i)\,. \tag{9}$$

The interaction term $(\partial \boldsymbol{v}_i/\partial t)_{\rm ww}$ describes the coupling of dust particles with cross section σ_i and mass m_i with gas of density ϱ and isothermal sound speed c_s.

2.2. *Fractal Grains*

2.2.1. *Mass-to-Radius Relation*

There is no simple relation between mass and radius for fractal grains as there is for compact spherical dust particles. Here a grain model that describes the transition from the compact constituent grains (at the lower radius limit of the size distribution) to the fractals (at the higher end) must be applied. For BPCA and BCCA grains Henning & Stognienko (1996) give an analytic expression for the filling factor f in relation to the extremal radius $r_{{\rm ex},i}$ of the grains:

$$m_i = \frac{4\pi}{3}\,\varrho_{\rm bulk}\,r_{{\rm ex},i}^3\,f_i\,, \tag{10}$$

$$f_i^{\rm PCA} = 0.0457\left[1 + 696\left(\frac{r_{{\rm ex},i}}{0.01\ \mu{\rm m}}\right)^{-3.93}\right], \tag{11}$$

$$f_i^{\rm CCA} = 0.279\left(\frac{r_{{\rm ex},i}}{0.01\ \mu{\rm m}}\right)^{-1.04} \times\left[1 + 4.01\left(\frac{r_{{\rm ex},i}}{0.01\ \mu{\rm m}}\right)^{-1.34}\right]. \tag{12}$$

The extremal radius $r_{{\rm ex},i}$ is defined as the radius of the minimal envelope sphere covering a fractal particle with bulk density $\varrho_{\rm bulk}$. The constituent grains are assumed to have radii of 0.01 μm.

2.2.2. *Opacities and Radiative Acceleration*

Dust opacities for coagulated grains, averaged over a given size distribution, have been calculated by Henning & Stognienko (1996). R. Schräpler et al. (2000, private communication), with the authors' permission, kindly provided us with their basic size-dependent specific extinction coefficients. We used the opacities for olivine ([Fe, Mg]$_2$SiO$_4$) dust grains (Fig. 2).

2.2.3. *Sticking of Grains*

In contrast to compact spherical grains, the fractal coagulates stick at their limb structures, which are built by the small constituent grains. The reduced radius R in equation (5) for the critical sticking energy must be calculated using the radii of these constituent grains. In this manner the formula for the sticking velocity by Chokshi et al. (1993) can be generalized to fractal particles (see § 2.1.2).

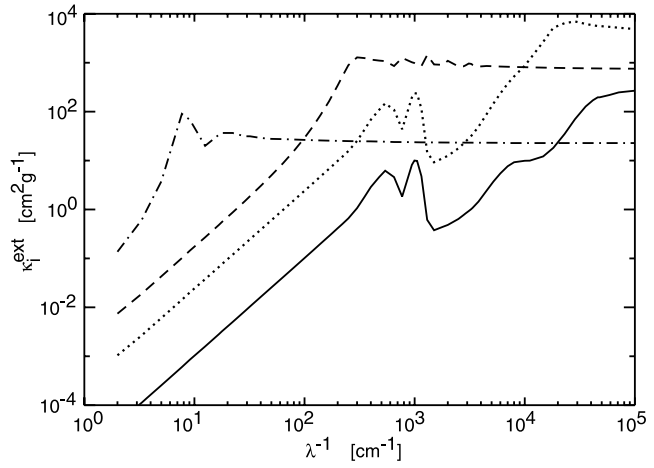

FIG. 2.—Specific extinction coefficient of fractal dust particles with sizes of 5 nm (*solid line*), 0.1 μm (*dotted line*), 5 μm (*dashed line*), and 0.2 mm (*dot-dashed line*).

2.2.4. *Grain Shattering*

Two approaches were followed. First, grain shattering is treated the same way as for the compact spherical grains. The analysis depends only on material parameters, the relative velocity, and the masses of the colliding particles. Although this assumption may seem inadequate, it poses an upper limit to the grains' resistance against shattering. Fractals seem to be rather fragile constructs with low binding energy when only van der Waals adhesion is considered. However, experimental studies show that fractal particles are always more resistant against destruction than the predictions of theoretical models (Poppe & Blum 1997; Wurm 1997). Fractals possess a multitude of vibrational excitation modes that provide a wide channel to dissipate the kinetic energy of the impacting grain.

As a second approach we adapt the shattering model of Dominik & Tielens (1997): the critical shattering velocity $v_{\rm crit}$ is proportional to the sticking velocity $v_{\rm stick}$ and the number of contact points between the two colliding grains. The values thus obtained are rather low compared to the model of Jones et al. (1996).

2.2.5. *Gas-Dust Interaction*

The gas-dust interaction also has to be modified as a result of the fractal structure of BPCA grains. In order to find an analytic expression for the effective cross section, Ossenkopf (1993) fitted numerical calculations of the cross section σ of coagulates in dependence of their compact volume V:

$$\frac{\sigma}{\sigma_0} = a\left(\frac{V}{V_0}\right)^{2/3} \exp\left[-\frac{b}{(V/V_0)^c}\right],$$

$$a = \begin{cases} 15.2\,, & 2 \le \dfrac{V}{V_0} \le 1000\,, \\ 4.7\,, & \dfrac{V}{V_0} > 1000\,, \end{cases}$$

$$b = \begin{cases} 2.86\,, & 2 \le \dfrac{V}{V_0} \le 1000\,, \\ 9.02\,, & \dfrac{V}{V_0} > 1000\,, \end{cases}$$

$$c = \begin{cases} 0.096\,, & 2 \le \dfrac{V}{V_0} \le 1000\,, \\ 0.503\,, & \dfrac{V}{V_0} > 1000\,. \end{cases} \tag{13}$$

For BCCA particles the following expression has been derived:

$$\frac{\sigma}{\sigma_0} = \begin{cases} \text{like BPCA} & \dfrac{V}{V_0} < 25\,, \\ 0.692\left(\dfrac{V}{V_0}\right)^{0.95}\left[1 + \dfrac{0.301}{\ln(V/V_0)}\right] & \dfrac{V}{V_0} \ge 25\,. \end{cases} \tag{14}$$

Here the normalization factors σ_0 and V_0 are the cross section and the volume of the (compact) constituent grains $\sigma_0 = \pi(0.01\ \mu\text{m})^2$ and $V_0 = (4\pi/3)(0.01\ \mu\text{m})^3$. The compact volume can be calculated using the filling factor of § 2.2.1. Thus, a relation between $r_{\rm ex}$ and the cross section σ of the grains can be established and used in the interaction term of § 2.1.4.

2.2.6. *Dust-Dust Interaction*

For the dust-dust interaction (coagulation) yet another radius definition has been introduced. The toothing radius $r_{\rm tooth}$ is defined as half the average distance of the center of mass of two sticking grains. It measures the penetration of two fractal grains and has been determined by Ossenkopf (1993) by fits to numerical calculations that simulated the scan of the "coastline" of the larger dust particle by the smaller one. Thus, the collisional cross section for grain-grain collisions $\sigma_{\rm coll}$ reads

$$\sigma_{\rm coll} = \sigma^{(1)}(1 - \zeta^2) + [4\pi - 8.3(1 - \zeta^{-1.22})][r_{\rm tooth}^{(2)}]^2\,, \tag{15}$$

with

$$\zeta = \frac{r_{\rm tooth}^{(2)}}{r_{\rm tooth}^{(1)}}\,, \tag{16}$$

$$r_{\rm tooth} = 0.72 V^{1/3} x^{0.21}\left(1 - \frac{0.216}{x^{1/3}}\right), \tag{17}$$

$$x = \frac{\sigma^3}{V^2}\,. \tag{18}$$

The superscripts (1) and (2) denote the grain with the larger and the smaller toothing radius, respectively.

2.3. *Coagulation and Shattering*

Adding the different source terms of grain acceleration, it becomes obvious that the dust particles will gain relative velocities to each other. The absolute values of these velocities depend on the dust absorption and scattering cross sections, the radiative flux, the gas density, and the specific cross section of the grains:

$$\left(\frac{\partial \boldsymbol{v}_i}{\partial t}\right) = \left(\frac{\partial \boldsymbol{v}_i}{\partial t}\right)_{\rm grav} + \left(\frac{\partial \boldsymbol{v}_i}{\partial t}\right)_{\rm rad} + \left(\frac{\partial \boldsymbol{v}_i}{\partial t}\right)_{\rm ww}$$
$$= -\nabla\Phi + \frac{\overline{\kappa}_i^p \boldsymbol{F}}{c} + \frac{4}{3}\,\varrho\,\frac{\sigma_i}{m_i}\sqrt{c_s^2 + (\boldsymbol{v} - \boldsymbol{v}_i)^2}$$
$$\times (\boldsymbol{v} - \boldsymbol{v}_i)\,. \tag{19}$$

In addition to these systematic relative velocities, a random contribution is caused by Brownian motion and turbulence. Because our hydrodynamical grid is too coarse to resolve typical turbulent length scales, and because turbulence needs a three-dimensional treatment, we apply a turbulence model developed by Völk et al. (1980). It is coupled to the turbulent angular momentum transport (Shakura & Sunyaev 1973) by the parameter α. Here the macroscopic turbulent velocity $v^0_{\rm turb}$ is set to a fraction α of the isothermal sound speed c_s, and the macroscopic revolution timescale $t^0_{\rm turb}$ is proportional to the orbital period Ω:

$$v^0_{\rm turb} = \alpha c_s \,, \tag{20}$$

$$t^0_{\rm turb} = \frac{2\pi}{\Omega} \,. \tag{21}$$

A Kolmogorov-type turbulence spectrum is assumed, whereby the turbulent energy is transported from the largest eddies down to the smallest at a constant rate. The corresponding scales of the smallest eddies are defined where the turbulent Reynolds number Re_s of the gas with viscosity η equals 1 (i.e., the flow becomes laminar; Lang 1974):

$$v^s_{\rm turb} = v^0_{\rm turb}\, \mathrm{Re}_0^{-1/4} \,, \tag{22}$$

$$t^s_{\rm turb} = t^0_{\rm turb}\, \mathrm{Re}_0^{-1/2} \,, \tag{23}$$

with

$$\mathrm{Re}_0 = \frac{\varrho v^0_{\rm turb} \lambda^0_{\rm turb}}{\eta} \approx \frac{\varrho (v^0_{\rm turb})^2 t^0_{\rm turb}}{\eta} \,. \tag{24}$$

The back-reaction of the gas turbulence on the dust particles depends on the coupling strength between grains and gas. This strength can be measured by the correlation timescale τ_i:

$$\tau_i = \frac{|\boldsymbol{v} - \boldsymbol{v}_i|}{(\partial v_i/\partial t)_{\rm ww}} \,. \tag{25}$$

According to the analytical fit of Weidenschilling (1984) to the numerical results of Völk et al. (1980), the random relative velocities between two grains with correlation timescales τ_1 and τ_2 ($\tau_1 \le \tau_2$) can be expressed as follows:

$$\delta v_{\rm turb} = \begin{cases} v^s_{\rm turb} \dfrac{|\tau_1 - \tau_2|}{t^s_{\rm turb}} & \text{if } \tau_1, \tau_2 \le t^s_{\rm turb} \,, \\ v^0_{\rm turb} & \text{if } \tau_1 \le t^0_{\rm turb} \le \tau_2 \,, \\ v^0_{\rm turb} \dfrac{t^0_{\rm turb}(\tau_1 + \tau_2)}{2\tau_1 \tau_2} & \text{if } t^0_{\rm turb} \le \tau_1, \tau_2 \,, \\ v^0_{\rm turb} \dfrac{3\tau_2}{\tau_1 + \tau_2} \sqrt{\dfrac{\tau_2}{t^0_{\rm turb}}} & \text{otherwise} \,. \end{cases} \tag{26}$$

The cutoff of the turbulent eddies at the lower size end of the eddy spectrum is included according to the considerations of Weidenschilling (1984). The contribution of Brownian motion to the random part of the relative velocities between dust grains is only important for small ($a_i < 1$ μm) grains:

$$\delta v_{\rm brown} = \sqrt{\frac{8kT}{\pi} \frac{m_i + m_j}{m_i m_j}} \,. \tag{27}$$

Thus, the dust particles achieve a total relative velocity $\delta v_{i,j} = (\delta v^2_{\rm syst} + \delta v^2_{\rm turb} + \delta v^2_{\rm brown})^{1/2}$, where $\delta v_{\rm syst}$ denotes the systematic relative velocities. These relative velocities are then evaluated according to the considerations of § 2.1 or § 2.2.

If the velocities are sufficiently low, the particles can coagulate. This is mathematically described by the coagulation equation:

$$\left[\frac{\partial n(m)}{\partial t}\right]_{\rm coag} = \frac{1}{2} \iint \alpha(m', m'') n(m') n(m'') \times \delta(m - m' - m'') dm' dm'' - n(m) \int \alpha(m, m') n(m') dm' \,, \tag{28}$$

with

$$\alpha(m', m'') = p \sigma_{\rm coll}(m', m'') \delta v(m', m'') \,. \tag{29}$$

The variables $n(m)$, $\sigma_{\rm coll}(m', m'')$, and $\delta v(m', m'')$ are the number density, the relative interaction cross section, and the relative velocity of grains with masses m, m', and m'', respectively. The sticking probability p controls the onset of bouncing when the relative velocities become too high ($p \to 0$). Grain shattering is described by a generalization of the above coagulation equation:

$$\left[\frac{\partial n(m)}{\partial t}\right]_{\rm shat} = \frac{1}{2} \iint \beta(m', m'') n(m') n(m'') \times \gamma(m, m', m'', \delta v(m', m'')) dm' dm'' - n(m) \int \beta(m, m') n(m') dm' \,, \tag{30}$$

with

$$\beta(m', m'') = q \sigma_{\rm coll}(m', m'') \delta v(m', m'') \,. \tag{31}$$

Here the function γ distributes the shattered dust fragments to the appropriate mass bins (see the Appendix). Again, the shattering probability q controls the onset of shattering above the critical velocity ($q \to 1$). The total dust evolution operator (coagulation/shattering) is the sum of both partial operators.

3. NUMERICAL TECHNIQUES

To simulate the collapse of a gravitationally unstable rotating molecular cloud core, we apply a multicomponent radiation hydrodynamics code with detailed dust dynamics (grain drift, coagulation, shattering). To keep the problem tractable, axial symmetry is assumed ("2.5 D" in cylindrical coordinates). An explicit nested grid technique is applied to resolve the inner parts of the accretion disk (Yorke & Kaisig 1995).

3.1. *Solution of the Coagulation/Shattering Equation*

To solve the combined coagulation/shattering equation numerically, the dust size distribution is binned into N discrete logarithmically spaced mass intervals. The continuous equation (§ 2.3) is therefore discretized:

$$\left(\frac{\partial n_k}{\partial t}\right) = \left(\frac{\partial n_k}{\partial t}\right)_{\rm coag} + \left(\frac{\partial n_k}{\partial t}\right)_{\rm shat} = \frac{1}{2} \sum_{i=1}^{N} \sum_{j=1}^{N} (\alpha_{ij} d_{ijk} + \beta_{ij} g_{ijk}) \times n_i n_j - n_k \sum_{i=1}^{N} (\alpha_{ik} + \beta_{ik}) n_i \,, \tag{32}$$

with

$$d_{ijk} = \begin{cases} \dfrac{m_i + m_j}{m_k} & \text{if } m_i + m_j \in [m_k^-, m_k^+] , \\ 0 & \text{otherwise} , \end{cases}$$

$$m_k^- = \frac{m_k + m_{k-1}}{2} \quad m_k^+ = m_{k+1}^- ,$$

$$g_{ijk} = \frac{m_i + m_j}{m_k} G_k(m_i, m_j, \delta v_{ij}) ,$$

$$G_k(m_i, m_j, \delta v_{ij}) \in [0, 1] ,$$

$$\sum_{k=1}^{N} G_k(m_i, m_j, \delta v_{ij}) = 1 . \tag{33}$$

The distribution of the shattered fragments is given by the discrete distribution function $G_k(m_i, m_j, \delta v_{ij})$ (see the Appendix). The kernels α_{ij} and β_{ij} are the discretized counterparts of $\alpha(m', m'')$ and $\beta(m', m'')$ (§ 2.3). Substituting backward time differences for all time derivatives, this nonlinear integrodifferential equation can be brought into the form

$$\frac{\boldsymbol{n}^* - \boldsymbol{n}}{\Delta t} = \mathscr{A}(\boldsymbol{n}^*)\boldsymbol{n}^* , \tag{34}$$

where $\boldsymbol{n} = (n_1, n_2, \ldots, n_N)$ are the (known) densities at the beginning of the time step and $\boldsymbol{n}^*$ are the corresponding values after time Δt that are to be determined. $\mathscr{A}(\boldsymbol{n}^*)$ is a matrix that is constructed from the right-hand side of equation (32). The advantages of backward time derivatives are (1) the difference equations are numerically stable for all choices of time steps Δt and (2) the numerical solution approaches the correct steady state solution as $\Delta t \to \infty$. We iteratively solve the implicit equation (34) for each cell in the numerical grid using a multidimensional Newton-Raphson algorithm. In order to optimize convergence, we adaptively reduce the time step with respect to the relatively large time step used for the explicit hydrodynamics. We tested our solver by calculating the solution of simple coagulation problems for which analytic solutions exist (Wetherill 1990). The correspondence was very good at high resolutions of mass binning. At resolutions comparable to those used in the collapse calculations the accuracy suffers. Sharply peaked mass distributions and discontinuous mass distributions become more diffuse with the passage of time. We do not consider this to be a serious flaw, however, because of the large uncertainties of the details of grain growth and destruction. The total mass of the dust component was always conserved within rounding errors (Suttner, Yorke, & Lin 1999).

3.2. *The Multicomponent Radiation Hydrodynamic Code*

An explicit/implicit method is used to solve the coupled hydrodynamic equations and the equations of radiation transport. The system is separated applying operator splitting, and the partial equations are then discretized explicitly or implicitly according to stability considerations. The dust size distribution is binned into N mass intervals and the hydrodynamic equations for mass and momentum conservation are computed for the gas component and for each binned dust component (grain size) simultaneously. The equations of mass conservation for gas (ϱ) and dust particles (ϱ_k) can be written as

$$\frac{\partial \varrho}{\partial t} + \nabla \cdot (\varrho \boldsymbol{v}) = 0 ,$$

$$\frac{\partial \varrho_k}{\partial t} + \nabla \cdot (\varrho_k \boldsymbol{v}) = -\varrho_k \sum_{i=1}^{N} (\alpha_{ik} + \beta_{ik}) \frac{\varrho_i}{m_i} + \frac{1}{2} \sum_{i=1}^{N} \sum_{j=1}^{N} (\alpha_{ij} d_{ijk} + \beta_{ij} g_{ijk}) \times \frac{\varrho_i}{m_i} \frac{\varrho_j}{m_j} m_k .$$

Here dust coagulation and shattering have been included in the equation of continuity for the dust particles as a source/sink term.

The equations for momentum conservation in cylindrical coordinates for gas and dust grains are

$$\frac{\partial(\varrho v_z)}{\partial t} + \nabla \cdot (\varrho v_z \boldsymbol{v}) = -\frac{\partial p}{\partial z} - \varrho \frac{\partial \Phi}{\partial z} + \varrho \sum_{k=1}^{N} I_k(v_{k,z} - v_z) - (\nabla \cdot \mathscr{Q}_{\rm visc})_z ,$$

$$\frac{\partial(\varrho v_r)}{\partial t} + \nabla \cdot (\varrho v_r \boldsymbol{v}) = -\frac{\partial p}{\partial r} - \varrho \frac{\partial \Phi}{\partial r} + \varrho \sum_{k=1}^{N} I_k(v_{k,r} - v_r) + \varrho \frac{v_\phi^2}{r} - (\nabla \cdot \mathscr{Q}_{\rm visc})_r ,$$

$$\frac{\partial(\varrho v_\phi r)}{\partial t} + \nabla \cdot (\varrho v_\phi r \boldsymbol{v}) = \varrho \sum_{k=1}^{N} I_k(v_{k,\phi} - v_\phi) r - (\nabla \cdot \mathscr{Q}_{\rm visc})_\phi r ,$$

$$\frac{\partial(\varrho_k v_{k,z})}{\partial t} + \nabla \cdot (\varrho_k v_{k,z} \boldsymbol{v}_k) = \varrho_k \frac{\overline{\kappa}_k^p F_z}{c} - \varrho_k \frac{\partial \Phi}{\partial z} - \varrho I_k(v_{k,z} - v_z) ,$$

$$\frac{\partial(\varrho_k v_{k,r})}{\partial t} + \nabla \cdot (\varrho_k v_{k,r} \boldsymbol{v}_k) = \varrho_k \frac{\overline{\kappa}_k^p F_r}{c} - \varrho_k \frac{\partial \Phi}{\partial r} - \varrho I_k(v_{k,r} - v_r) + \varrho_k \frac{v_{k,\phi}^2}{r} ,$$

$$\frac{\partial(\varrho_k v_{k,\phi} r)}{\partial t} + \nabla \cdot (\varrho_k v_{k,\phi} r \boldsymbol{v}_k) = -\varrho I_k(v_{k,\phi} - v_\phi) r ,$$

with the interaction term

$$I_k = \frac{4}{3} \varrho_k \frac{\sigma_k}{m_k} \sqrt{c_s^2 + (\boldsymbol{v} - \boldsymbol{v}_k)^2} . \tag{35}$$

The advection part of these equations is solved by an explicit second-order scheme. The gas-dust interaction terms need an implicit treatment because of the stiffness of the problem.

The tensor $\mathscr{Q}_{\rm visc}$ that appears in several of the above equations denotes the viscous stress tensor of the α-viscosity (Shakura & Sunyaev 1973):

$$\mathscr{Q}_{\rm visc} = \varrho \nu \boldsymbol{e} , \tag{36}$$

where e is the shear tensor. In addition, ν is calculated from

$$\nu = \alpha c_s H \approx 0.7 \frac{\alpha c_s^2}{\Omega} , \tag{37}$$

where the density scale height H has been replaced by an expression valid for equilibrium "thin" disks. For the calculation described in this study both sound speed c_s and angular velocity Ω are approximately constant along the surfaces of cylinders within the equilibrium disk (see the theoretical discussion in Tassoul 1978). Thus, ν varies principally as a function of the radial distance within the disk.

The viscosity as described above is applied to the entire grid. Within the accretion disk it modifies the flow by allowing angular momentum to be transferred radially outward within the disk. The parameter α is continuously adjusted according to the Toomre stability criterion and is allowed to vary within the range of 10^{-3} to 0.1 (see Yorke & Bodenheimer 1999). We define the Toomre parameter $Q_{\rm T}$ within the accretion disk for each time step by the minimum value of

$$Q_{\rm T} = \min_{r \le R_{\rm disk}} \left(\frac{\Omega c_s}{\pi G \Sigma} \right)_{z=0} , \tag{38}$$

where $\Sigma(r) = \int \varrho \, dz$ is the disk's surface density. If $Q_{\rm T}$ drops below 1.3 (i.e., nonradial instabilities can be expected to occur), we increase α by a small factor (typically 1.002), if necessary to its maximum value 0.1. If $Q_{\rm T}$ increases above 1.5 (the disk becomes stable), α is reduced by a small factor (typically 0.999). Generally, $Q_{\rm T}$ "hovers" at either 1.3 or 1.5, and α levels off at values somewhere between $\alpha \approx 0.01$ (for $M = 1\ M_\odot$) and $\alpha \approx 0.08$ (for $M = 10\ M_\odot$).

Radiation transport is calculated within the framework of the gray flux-limited diffusion approximation (Levermore & Pomraning 1981; Yorke & Bodenheimer 1999):

$$\frac{\partial a T_d^4}{\partial t} = \nabla \cdot \left[\frac{c \lambda_R \nabla a T_d^4}{\sum_{k=1}^N \overline{\kappa}_k(T_d) \varrho_k} \right] + L_* \, \delta(V_1) = 0 , \tag{39}$$

with flux limiter λ_R, Rosseland mean opacity $\overline{\kappa}_k(T_d)$, the radiation constant a, and luminosity of the central source L_* (treated as an additional source term within the volume V_1 of the innermost grid cell):

$$\delta(V_1) = \begin{cases} \dfrac{1}{V_1} & \text{if innermost cell} , \\ 0 & \text{otherwise} , \end{cases} \tag{40}$$

$$\lambda_R = \frac{1}{\xi} \left[\coth(\xi) - \frac{1}{\xi} \right] , \tag{41}$$

$$\xi = \frac{|\nabla T_d^4|}{T_d^4 \sum_{k=1}^N \overline{\kappa}_k^{\rm ext}(T_d) \varrho_k} , \tag{42}$$

$$\frac{1}{\overline{\kappa}_k(T)} = \frac{\int_0^\infty (1/\kappa_{\lambda,k}^{\rm ext})(dB_\lambda/dT) d\lambda}{\int_0^\infty (dB_\lambda/dT) d\lambda} . \tag{43}$$

Here $B_\lambda = B_\lambda(T)$ is the Planck function. Because we are considering gray radiation transfer only, the equilibrium temperature of each dust grain is identical to the radiation temperature T_d. To solve equation (39) for T_d, an alternating direction implicit (ADI) procedure is used (Douglas & Rachford 1956).

By contrast, the gas is poorly coupled to the radiation field as a result of its low opacity. The dust grains interact with the gas by inelastic collisions that contribute a cooling term Λ to the equation for the internal energy density of the gas. The dissipation of viscous energy leads to an additional gas heating term $\mathcal{Q}_{\rm visc} : \nabla \boldsymbol{v}$,

$$\frac{\partial \epsilon}{\partial t} + \nabla \cdot (\epsilon \boldsymbol{v}) = -p \nabla \cdot \boldsymbol{v} - \Lambda(\varrho, \varrho_k, T, T_d) + \mathcal{Q}_{\rm visc} : \nabla \boldsymbol{v} . \tag{44}$$

Assuming an energy transfer of $k(T_d - T)$ per collision of a gas molecule with a dust grain, the cooling function becomes (μ_0 is the mean molecular weight of the gas)

$$\Lambda(\varrho, \varrho_k, T, T_d) = \frac{\varrho}{\mu_0 m_{\rm H}} \sum_{k=1}^N \frac{\varrho_k}{m_k} \sigma_k \sqrt{\frac{8kT}{\pi \mu_0 m_{\rm H}}} \, k(T_d - T) . \tag{45}$$

The equation of state $p(\varrho, T)$ and the internal energy $\epsilon(\varrho, T)$ for the gas component assume molecular gas and include dissociation of the H_2 molecules above ≈ 2000 K (Black & Bodenheimer 1975).

Finally, the gravitation potential of the molecular cloud is calculated by a solution of the Poisson equation, again using ADI:

$$\Delta \Phi = 4\pi G (\varrho + \sum_{k=1}^N \varrho_k) . \tag{46}$$

4. INITIAL AND BOUNDARY CONDITIONS

We start the numerical simulations with an isothermal, uniformly rotating molecular cloud core with a total mass of 1–10 $M_\odot$, a radius of $r = 2 \times 10^{16}$ cm, and a temperature of $T = 20$ K. This gives an initial free-fall timescale $t_{\rm ff}$ between ≈ 8600 and ≈ 2700 yr for these configurations. The angular velocities Ω range between 10^{-12} and 5×10^{-12} s^{-1} (see Table 1). We consider centrally peaked mass distributions $\varrho \propto 1/(r^2 + z^2)$. The total mass contribution of the dust grains is set to a fraction of 0.25×10^{-2} of the gas mass (corresponding to the mass contribution of silicates).

At the outer boundary of the space integration domain $[(r^2 + z^2)^{1/2} = 2 \times 10^{16}$ cm] the hydrodynamic variables are held constant (no inflow or outflow). This corresponds

TABLE 1

INITIAL CONDITIONS

Model	Dust	M_c ($M_\odot$)	Ω (10^{-12} s^{-1})	$t_{\rm ff}$ (yr)
1MS	Comp.	1	1	8635
3MS	Comp.	3	3	4985
5MS	Comp.	5	4	3870
10MS	Comp.	10	5	2730
1MS_PCA	BPCA	1	1	8635
3MS_PCA	BPCA	3	3	4985
5MS_PCA	BPCA	5	4	3860
10MS_PCA	BPCA	10	5	2730
1MS_CCA	BCCA	1	1	8635
3MS_CCA	BCCA	3	3	4985
5MS_CCA	BCCA	5	4	3860
10MS_CCA	BCCA	10	5	2730

NOTE.—M_c: mass of cloud core; Ω: angular velocity; $t_{\rm ff}$: free-fall timescale.

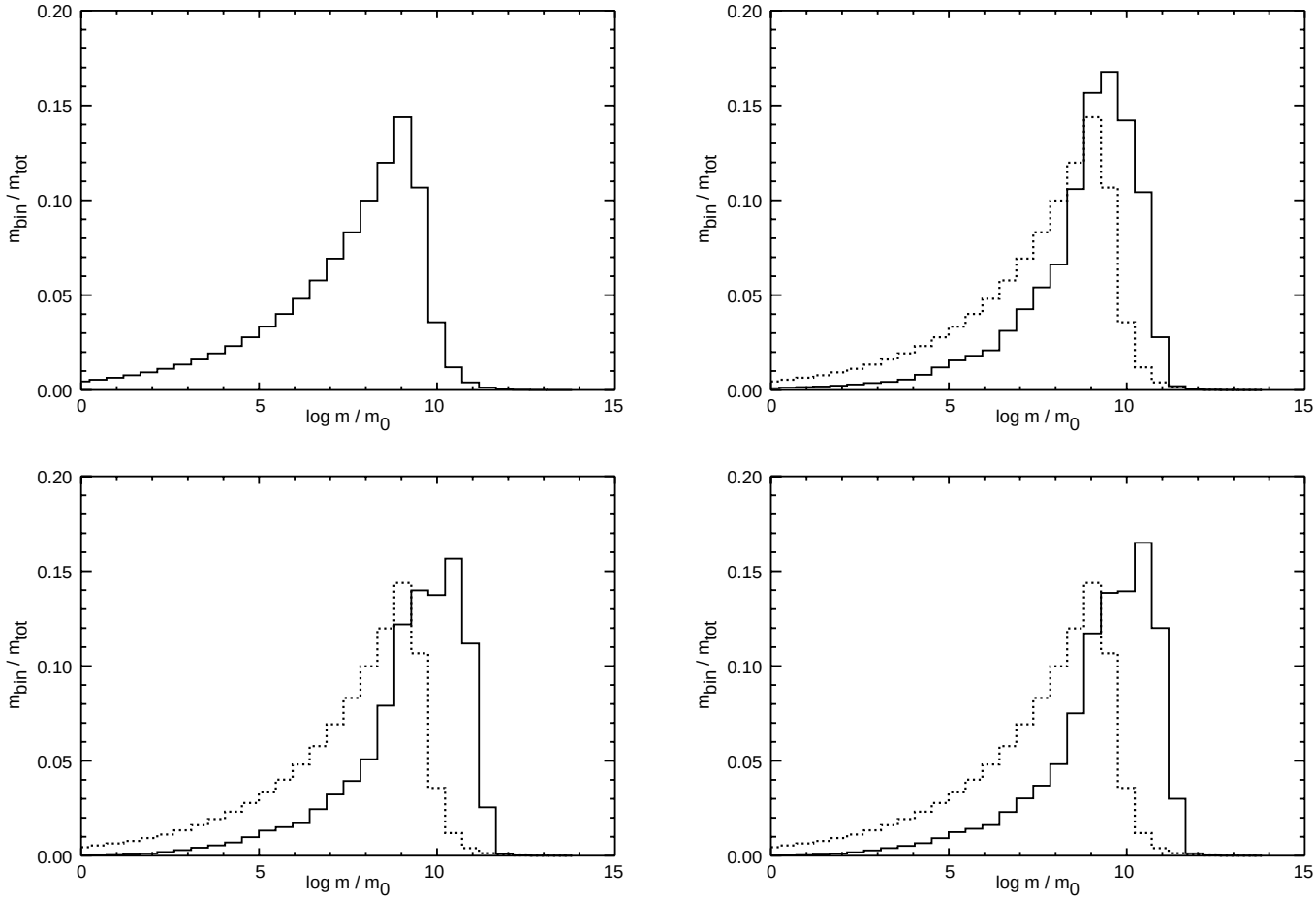

FIG. 3.—Evolution of the total dust mass distribution for the times shown in Fig. 5

to an assumption that no material from the parent cloud will enter into the portion undergoing collapse. This does not mean that the mass influx rate of dusty material onto the new formed disk is suddenly cut off after one free-fall time. Instead, it steadily decreases as the material in the outer zones, initially slowed by pressure gradients in the density-peaked distribution, is depleted (see Yorke & Bodenheimer 1999). Even after three free-fall times, there is an appreciable mass influx onto the disk. From other studies (e.g., Mizuno et al. 1988) we know that if the enshrouding molecular cloud can continuously supply small dust grains, the grain size distribution will be affected. This effect will be present to some extent in the studies discussed here. The issue of the time dependency of the mass

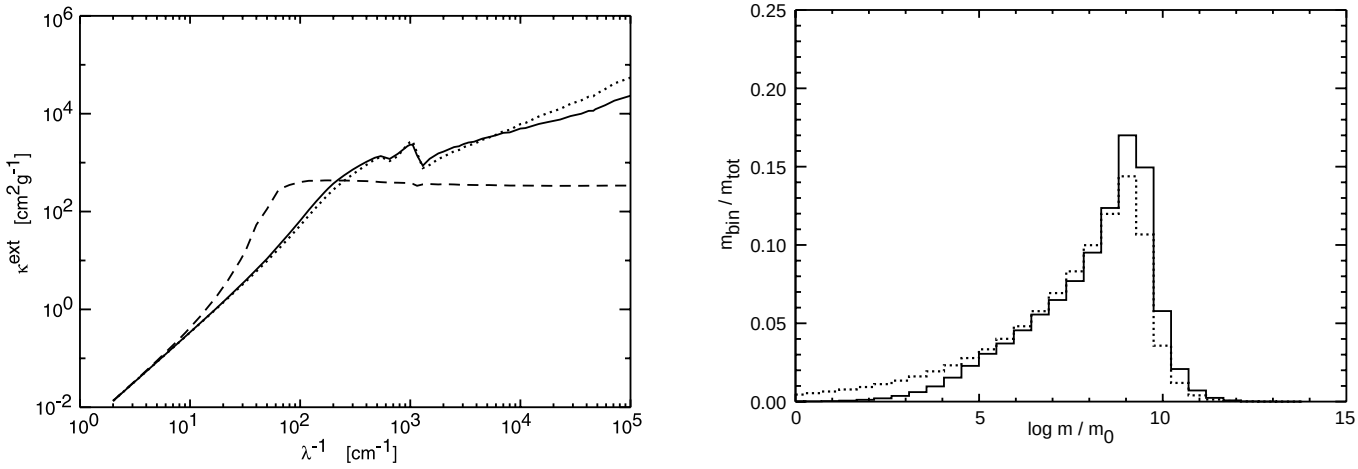

FIG. 4.—Model 3MS, 11,400 yr. *Left:* Specific extinction coefficient of the dust in the accretion shock (*dotted line*) and in the equatorial plane of the accretion disk (*dashed line*) is compared with an MRN77 mass distribution (*solid line*). *Right:* Overall mass spectrum at the end of a comparison simulation whereby the contribution of systematic velocities to the relative motion of the dust grains is neglected.

influx is a nontrivial one, however, and is beyond the scope of the present investigation.

The particle sizes are distributed according to an MRN77 power law with an exponent of -3.5, which can be transformed to a bin mass distribution $m_{\rm bin}(m_k)$:

$$n(a) \propto a^{-3.5}\,, \tag{47}$$

$$m_{\rm bin}(m) d\ln m \propto m^{1/6} d\ln m\,, \tag{48}$$

with grain mass m. Figure 3 (*upper left panel*) shows the initial MRN77 dust mass distribution. On a logarithmic scale the dust mass increases with increasing bin mass. The grain sizes range from 5 nm to 5 μm at the beginning. Above 5 μm the particle density falls off proportionally to $m_{\rm bin}^{-1}$ [this corresponds to $n(a) \propto a^{-7}$]. The dynamics of these large grains at the upper end of the computed size distribution can be followed throughout the simulation without being relevant for coagulation (provided that the upper end is chosen far enough away from the largest particles produced by coagulation). The integration domain in dust size space ranges from 5 nm up to 0.2 mm, which spans about 14 orders of magnitude in grain mass. Whenever the dust temperature is low enough to allow an ice coating on the grains' surfaces, the sticking probabilities are modified accordingly.

The innermost cell of the finest grid contains the central protostellar source and requires special treatment. Its total luminosity L_* can be approximated by the sum of the core's intrinsic luminosity and the luminosity due to accretion of material onto the core:

$$L_* = 3L_\odot \left(\frac{M_*}{M_\odot}\right)^3 + \frac{3}{4}\frac{GM_*\dot{M}_*}{R_*}\,. \tag{49}$$

The radius R_* of the central object is held constant at 10 $R_\odot$. $\dot{M}_*(t)$ and $M_*(t) = \int \dot{M}_*\, dt$ result from the calculations.

Figure 4 (*left panel, solid line*) displays the net specific extinction coefficient for a gas-dust mixture with compact spherical grains. The opacities are calculated for the MRN77 mass distribution shown in Figure 3 (*upper left panel*). Because the dust opacities are calculated using the actual grain size distribution, they vary as a function of time and location during the simulation.

5. NUMERICAL SIMULATIONS

The following numerical calculations were conducted with three nested grids of increasing resolution of factor 2 each. The individual grids span 60×60 zones. The dust size distribution is sampled by $N = 30$ discrete dust species. Table 2 summarizes selected results of the simulations.

5.1. *Compact Spherical Dust Grains*

The first simulation applies the simple "compact spherical grain" dust model (§ 2.1). The collapse of the rotating molecular cloud core is followed for about 10^4 yr (about two initial free-fall times). Figure 5 displays an evolutionary sequence of the gas density and the gas velocity and Figure 3 the corresponding total grain mass spectrum.

As evident in the bottom panel of Figure 5, two accretion shock fronts have developed around the protostellar disk. The central mass and core luminosity have attained values of 2.2 $M_\odot$ and 87 $L_\odot$, respectively. As shown in Figure 3, coagulation removes the small dust particles effectively from the size distribution. At the high-mass end dust grains of ~ 50 μm are grown by coagulation. However, larger particles do not form during the simulation. The integral size distribution between 5 nm and 5 μm varies as $n(a) \propto a^{-3.1}$.

TABLE 2

SELECTED RESULTS

Model	M_* ($M_\odot$)	L_* ($L_\odot$)	M_d/M_*	$t_s/t_{\rm ff}$
1MS	0.77	3.7	0.30	2.5
3MS	2.2	87	0.36	2.3
5MS	3.7	194	0.35	2.1
10MS	8.2	1839	0.22	1.9
1MS_PCA	0.77	4.0	0.30	2.5
3MS_PCA	2.3	59	0.30	2.3
5MS_PCA	3.7	270	0.35	2.2
10MS_PCA	7.9	1639	0.27	2.2
1MS_CCA	0.77	2.9	0.30	3.1
3MS_CCA	2.2	80	0.36	2.5
5MS_CCA	3.8	188	0.32	2.3
10MS_CCA	8.0	1614	0.25	2.2

NOTE.—M_* and L_*: mass and luminosity of the central star; M_d: mass of disk; t_s: duration of simulation.

Figure 6 (*left panel*) shows the dust mass spectrum at selected heights above the protostellar accretion disk for a cylindrical distance of 30 AU. At the disk midplane (*right panel*) coagulation is very strong. Large grains are produced at the cost of the small-size end of the particle spectrum. At disk radii larger than about 200 AU the effect of coagulation becomes less important. Only the small grains are removed from the size spectrum by coagulation. However, in the accretion shock just above the disk (Fig. 6, *left panel*) the large grains are depleted relative to the low-mass dust particles.

The velocities of selected dust grains through the accretion shock at $r = 30$ AU (Fig. 7, *left panel*) show that dust grains of radii ≈ 1 μm and above are coupled only loosely to the gas so that significant relative velocities of several kilometers per second between these grains and the smaller ones are achieved. This implies that coagulation is inhibited and shattering might occur (the threshold velocity is 2.7 km s^{-1}). The densities are so low, however, that the shattering timescale is $\sim 10^4$ yr. Thus, the depletion of the large grains must be attributed to the fact that they pass quickly through this zone, whereas the smaller grains slow down significantly. This size-dependent gas-grain drift lowers the dust-to-gas mass ratio by more than a factor of 2 between the two accretion shocks (shown for the BPCA fractals; see Fig. 8, *right panel*).

Note the differing velocities above the outer accretion shock ($z \approx 170$ AU), caused by the size dependence of the grain opacity and thus by differential radiative acceleration. Without radiative acceleration the grains should fall toward the equatorial plane faster than the gas because they are not pressure supported. Outside the outer accretion shock the grains' mass distribution is still well approximated by the initial MRN77 mass distribution (Fig. 6, *left panel*). In outer regions of the cloud at the equatorial plane the infalling material is shielded from the central star by the disk. Hence, the grains do indeed accrete with higher velocities than the gas component (Fig. 7, *right panel*).

To quantify the effect of a modified dust size spectrum on the optical properties of the protostellar matter in the accretion disk, Figure 4 (*left panel*) compares the net specific

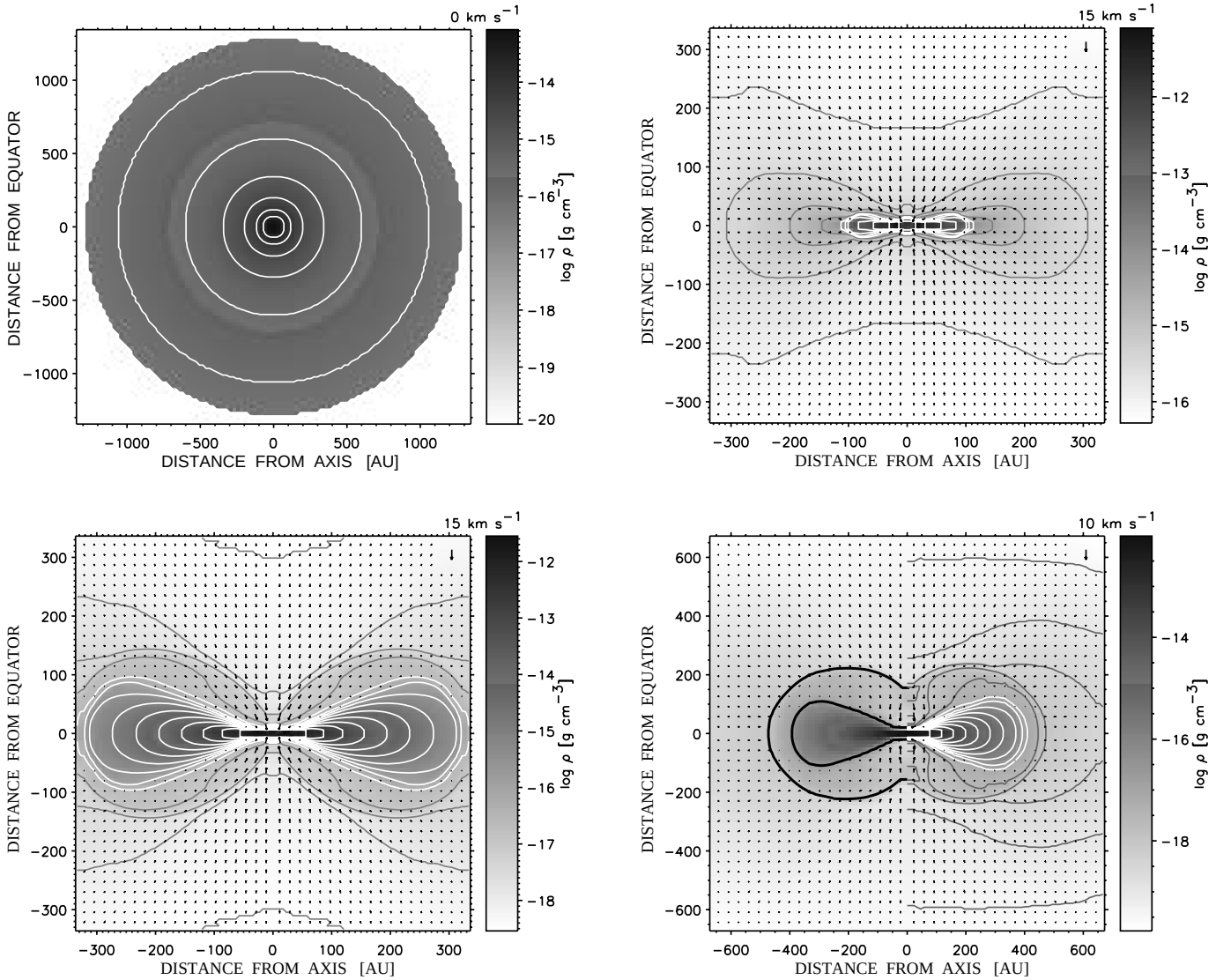

FIG. 5.—Evolution of density and velocity using the compact sphere dust model 3MS. Density contour lines are separated by $\Delta \log \varrho = 0.5$. From left to right and top to bottom the following times are shown: 0, 5100, 10,300, and 11,400 yr. In the bottom panel the locations of the accretion shocks are given by thick dark lines on the left half, where the density contour lines (shown on the right half only) begin to bunch tightly. The inner accretion shock encompasses the equilibrium accretion disk, where the (v_r, v_z) components of velocity are negligible. The outer accretion shock is less apparent because the bunching of a mere two contour lines, corresponding to a jump in density by a factor of ~ 10, is less conspicuous.

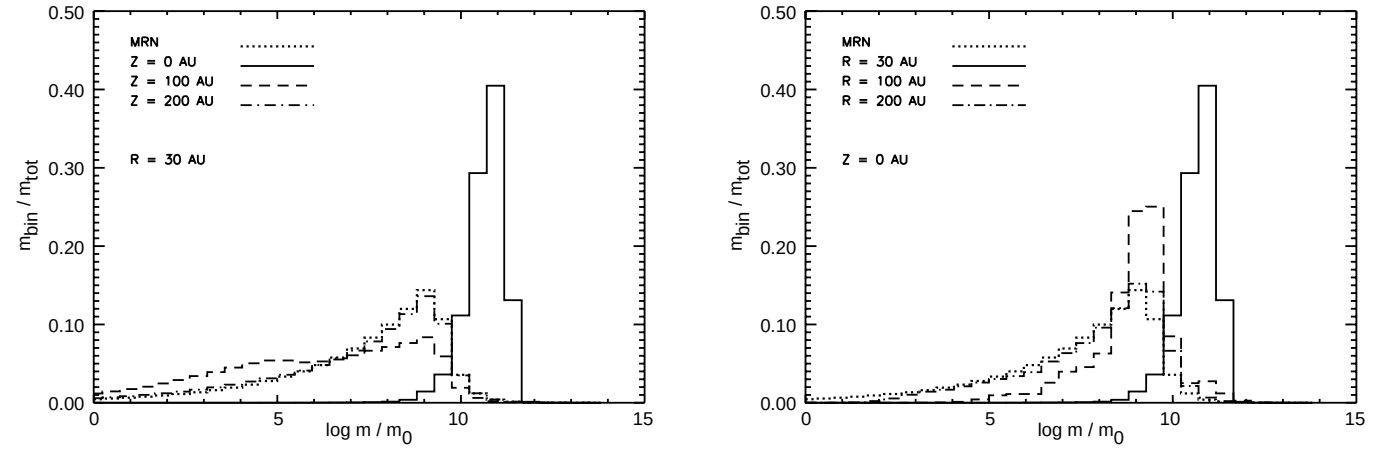

FIG. 6.—Model 3MS, 11,400 yr. *Left:* Dust mass distribution at selected heights above the disk's midplane for $r = 30$ AU. *Right:* Dust mass distribution at selected radial distances for $z = 0$ AU.

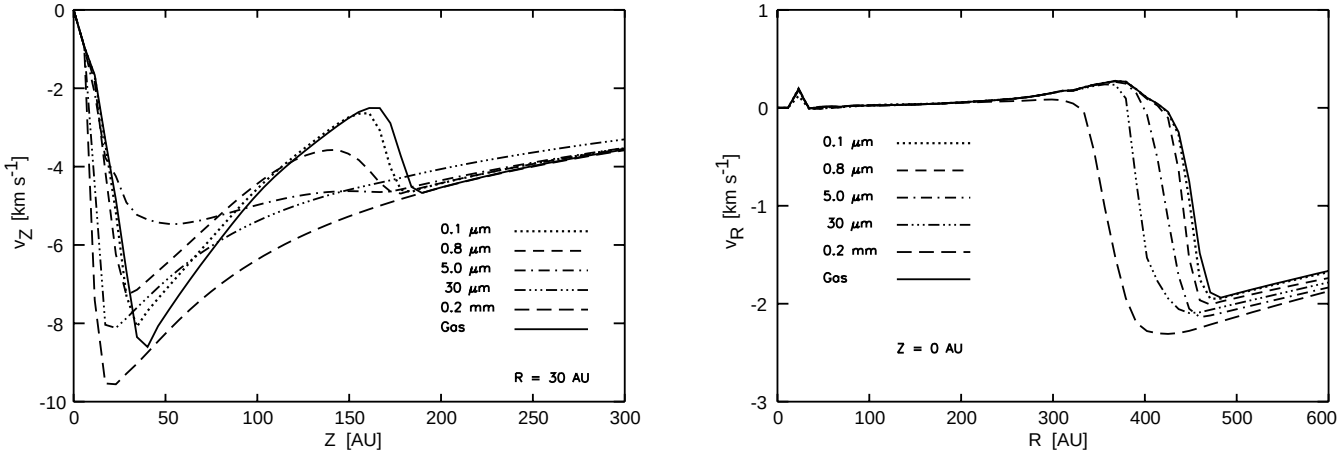

FIG. 7.—Model 3MS, 11,400 yr. *Left:* Vertical components of velocity of selected dust components at $r = 30$ AU. *Right:* Radial velocities of selected dust components in the equatorial plane ($z = 0$ AU).

extinction coefficient for several locations in the accretion disk. Whereas the depletion of the large grains behind the accretion shock does introduce minor modifications to the extinction coefficient, coagulation at the disk's midplane causes an opacity reduction of more than an order of magnitude for the near-infrared to UV extinction. From $\lambda = 0.1$ cm to 0.1 mm the extinction coefficient is increased by approximately the same amount. This behavior is indicative of the migration of the peak of the grain mass distribution to higher masses due to coagulation.

To drive the coagulation beyond the initial upper grain size limit of 5 μm, systematic relative velocities are needed, such as those that result from differential radiative acceleration, relaxation behind the accretion shock, and gravitative sedimentation. Figure 4 (*right panel*) displays the resulting dust mass distribution, when these contributions to the relative motions are neglected. Obviously, turbulence and Brownian motion are sufficient to remove the small grains, but they are not able to build up micron-sized particles quickly. Whereas for cloud clump masses of 1 $M_\odot$ the differential radiative acceleration of grains is negligible, it eventually becomes the most important mechanism for creating velocity differences between grains outside the accretion shock fronts when larger clump masses are considered.

5.2. *Influence of the Sticking Properties of the Grains*

How is coagulation affected by the sticking strength of the dust particles? As pointed out in § 1, this material property is not yet well understood. Reports on experimental studies indicate larger values for the critical sticking velocity than theoretical models predict (Poppe & Blum 1997). Ices on the grain surfaces play an important role (Supulver et al. 1997). To investigate this effect, we conducted comparison simulations with different sticking strengths. First, the critical sticking velocities were reduced to the conservative theoretical values (without the factor 10 correction for the experimental results; see § 2.1.2).

Figure 9 (*left panel*) displays the total mass distribution. Obviously, grain growth is reduced; the maximum grain mass is smaller by a factor of about 10. When the critical sticking velocity is set to infinity, i.e., the grains stick at every encounter, grains up to the actual bin limit with radii

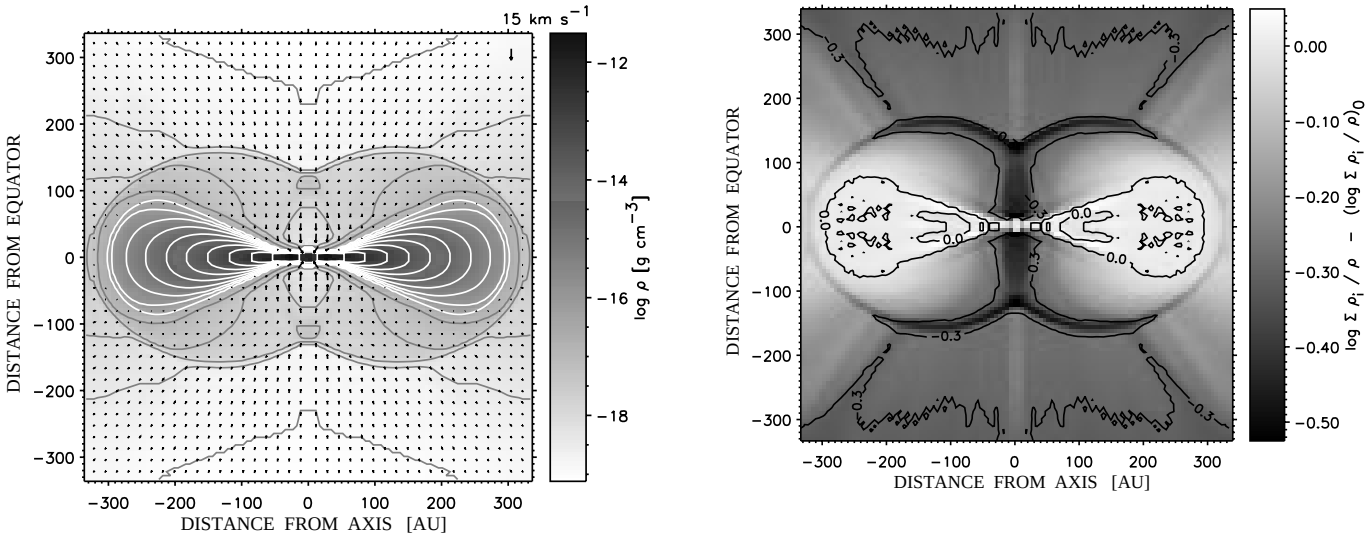

FIG. 8.—Model 3MS_PCA, 11,400 yr. *Left:* Mass density and velocity of the gas component. Symbols and contour lines are as in Fig. 5. *Right:* Variation of the dust-to-gas mass ratio in the accretion disk. $(\sum \varrho_i/\varrho)_0$ is the initial value. The outer accretion shock (bunching of approximately two contour lines in the left frame; surface of low dust-to-gas mass ratio in the right frame) at $z \approx \pm 125$–150 AU is readily discernible.

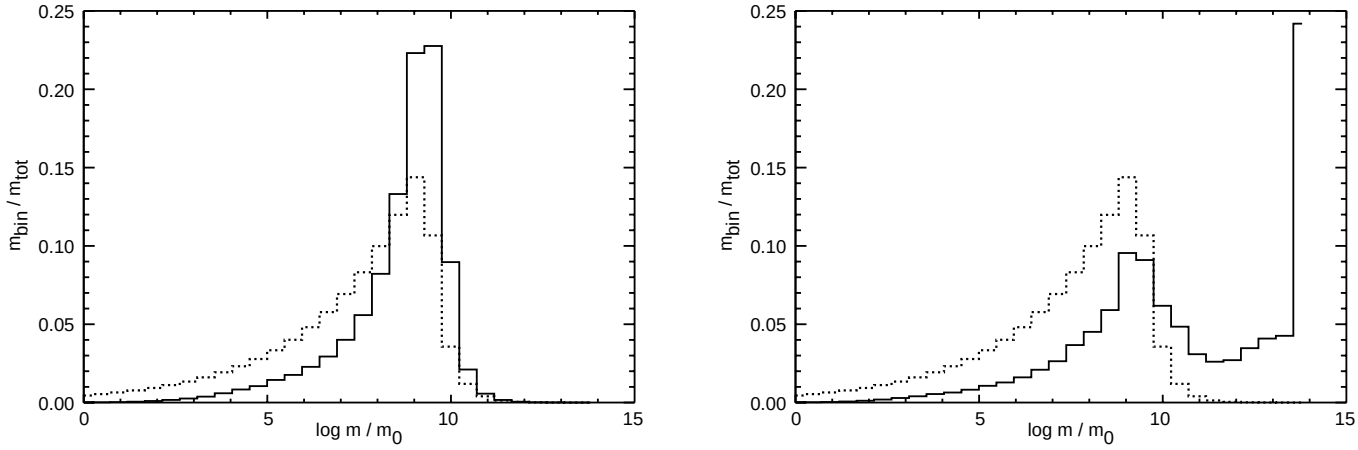

FIG. 9.—Overall mass spectrum of the grains (*solid lines*) compared to the initial MRN77 mass distribution (*dotted lines*). *Left:* The critical sticking velocity is reduced by a factor of 10 compared to model 3MS. *Right:* For comparison, the critical sticking velocity is set to infinity.

of about 0.2 mm are grown. This demonstrates that the material parameters play an extremely important role in defining the upper mass limit up to which the dust grains are able to grow during the formation of an accretion disk.

5.3. *Fractal BPCA Particles*

Our next approximation treats the dust grains as fractal coagulated particles (BPCA particles). The same initial and boundary conditions as in the previous calculation are used. At the end of the simulation the mass of the central object is 2.3 $M_\odot$ with a luminosity of 59 $L_\odot$. The overall evolution is qualitatively similar to the calculation with compact dust grains (Figs. 3 and 5). Figure 8 shows the mass density and velocity of the gas component (*left panel*) and the dust-to-gas mass ratio (*right panel*). Again, an accretion shock has developed. In this accretion shock the dust-to-gas mass ratio is reduced by a factor of about 3 compared to the initial value as a result of size-dependent advection.

The specific cross section of large BPCA coagulates is about a factor of 5 larger than for compact spheres of the same mass (§ 2.2). Only particles with radii of about 10 μm and larger decouple from the motion of the gas flow in the accretion shock (Fig. 10, *left panel*; compare to Fig. 7). Coagulation in the equatorial plane proceeds at a rate similar to the simple compact spherical dust model (Fig. 10, *right panel*). As in the case of spherical grains, no dust particles larger than several times 10 μm are grown by coagulation. This can be attributed again to a finite critical sticking velocity (see § 5.2).

5.4. *Fractal BCCA Particles*

Finally, BCCA grains are the most fluffy particles dealt with in these simulations. Figure 11 (*top panel*) shows the density and the velocity of the gas component in model 3MS_CCA. The overall distribution is similar to the previously discussed models (3MS and 3MS_PCA). However, grain coagulation is enormously strong. Grains as large as 0.2 mm (at the limiting end of the binning) are grown (Fig. 11, *bottom panel*). Almost all the grain mass resides in the most massive bin. Because of the fluffy structure of the BCCA grains, the dust remains well coupled to the gas, even in the accretion shock (Fig. 12, *left panel*). Thus, relative velocities between the dust particles remain very low.

The optical properties of the gas-dust mixture at several locations in the accretion disk are plotted in Figure 12 (*right panel*). In the equatorial plane the net specific extinction coefficient $\kappa_\lambda^{\rm ext}$ is lowered by more than an order of magnitude from the near-infrared to UV wavelengths. From 1 mm to 100 μm the extinction is enhanced. In the accretion shock

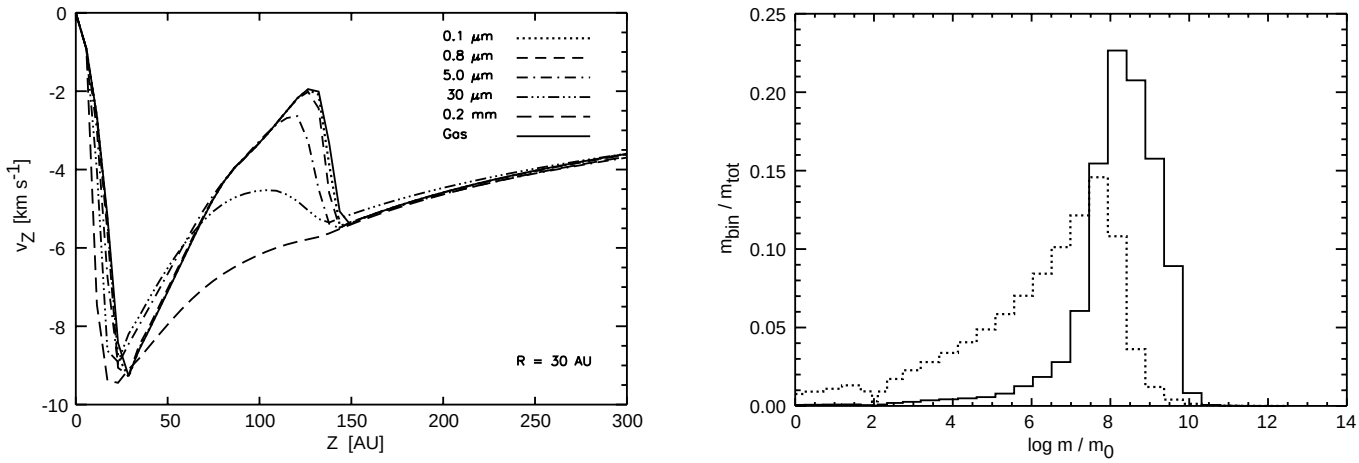

FIG. 10.—Model 3MS_PCA, 11,400 yr. *Left:* Vertical components of velocity of selected dust components at $r = 30$ AU. *Right:* Overall mass spectrum of the coagulated dust grains (*solid line*) compared to the initial MRN77 mass distribution (*dotted line*).

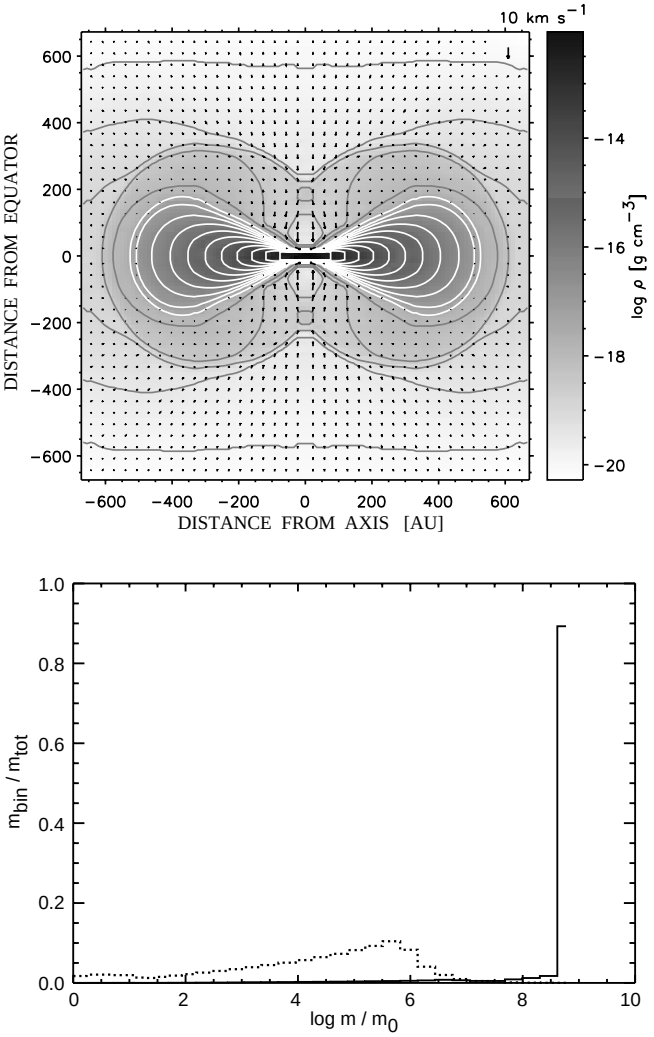

FIG. 11.—Model 3MS_CCA, 12,600 yr. *Top:* Gas density and velocity structure. *Bottom:* Overall mass spectrum of the coagulated dust grains (*solid line*) compared to the initial MRN77 mass distribution (*dotted line*).

only minor modifications can be ascertained.

A theoretical shattering model differing somewhat from the one discussed above has been developed by Dominik & Tielens (1997). In order to test its effect on our simulations, we used this model to compute the evolution of BCCA grains. According to Dominik & Tielens (1997), the shattering velocity is proportional to the critical sticking velocity. It also depends on the number of contact points between the two colliding dust grains. In our ignorance of this quantity we assume that two dust grains always have 10 contact points. Figure 13 (*top panel*) displays the density and velocity of dust grains with reduced radii $r_{ex} = 5$ μm. In the accretion shock near to the axis of rotation these dust particles are destroyed by shattering encounters. As can be seen in the total dust mass distribution (Fig. 13, *bottom panel*), the largest dust grains with radii of 0.2 mm are not formed. We attribute this to frequent shattering encounters; the sticking properties are identical to those used in model 3MS_CCA.

5.5. *Synthetic Emission Maps and Spectra*

In order to compare our numerical results to observations of young protostellar accretion disks, we have produced emission maps and spectra calculated with a "numerical telescope," which includes the contribution of scattered light (Yorke & Bodenheimer 1999). Figure 14 (*left panel*) shows the dust continuum emission at 3.6 μm at the final stage of the collapse of the "compact sphere" dust model (3MS). A dark bar across the midplane of the accretion disk marks a region of high extinction. Above and below the disk scattered light reveals the presence of the central protostellar radiation source. The spectral energy distribution (SED) shown in Figure 15 (*left panel*) displays well-known features of young dusty protostellar cores (e.g., Sonnhalter, Preibisch, & Yorke 1995): no direct radiation from the protostar (at an angle of 85°), a silicate absorption feature at $\lambda \approx 10$ μm, and a dust emission temperature of about 100 K. For comparison, the corresponding SED was recalculated for dust with an MRN77 mass distribution using the same density distribution. No obvious differences to the results using the more detailed coagulated dust model are detectable. This can be attributed to the fact that the strongly coagulated dust particles are embedded deeply within the accretion disk, whereas the outer layers contain only slightly modified grains. However, when all dust grains are assumed to have a radius of $a = 22$ μm (which corre-

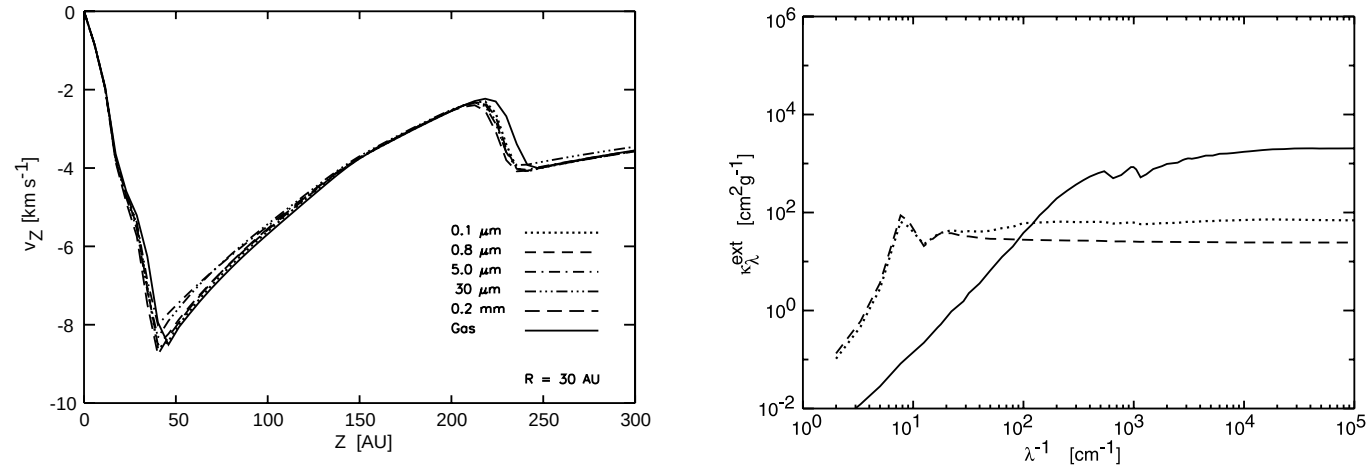

FIG. 12.—Model 3MS_CCA, 12,600 yr. *Left:* Vertical components of velocity of selected dust particles at $r = 30$ AU. *Right:* Net specific extinction coefficient of unmodified dust (*solid line*) compared to the numerical results for the equatorial midplane at $r = 300$ AU (*dotted line*) and $r = 30$ AU (*dashed line*).

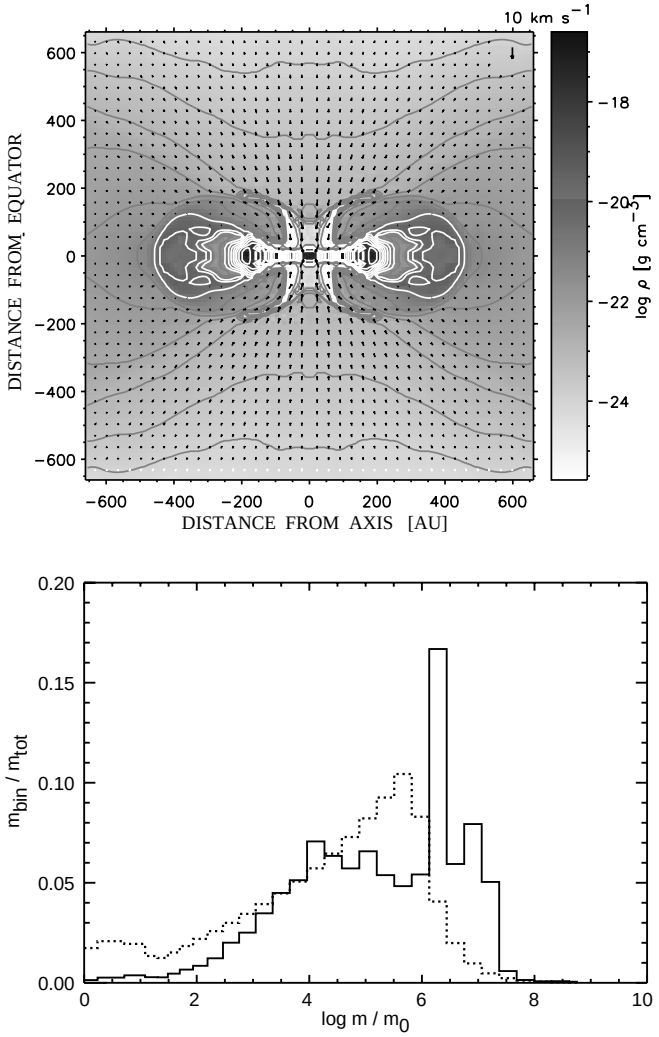

FIG. 13.—Model 3MS_CCA_S10, 12,700 yr. *Top:* Mass density and velocity of dust particles with $r_{ex} = 5$ μm. *Bottom:* Overall mass spectrum of the coagulated dust grains (*solid line*) compared to the initial MRN77 mass distribution (*dotted line*).

sponds to the maximum grain size formed in model 3MS), the calculated SED is markedly different from that resulting from dust with an MRN77 mass distribution. The silicate absorption feature is totally absent, and more near-infrared emission reaches the observer.

For comparison, an emission map using the unmodified MRN77 dust distribution has been calculated and displayed in Figure 14 (*right panel*). The differences are not overwhelming, but some general tendencies can be ascertained: for unmodified dust the dark absorption bar across the disk is somewhat more prominent (especially toward the edges of the disk), and more scattered light above and below the disk is visible. Because almost no coagulation occurred in these outer disk regions over the time period investigated, these differences result primarily from the differential advection of dust grains.

A similar tendency can be seen for the fractal grains. In Figure 16 (*left panel*) the continuum emission for simulation 3MS_CCA is displayed. In contrast to model 3MS, the dark absorption bar across the disk is far more transparent at $\lambda = 3.6$ μm when dust coagulation is permitted. When compared to the emission map resulting from uncoagulated dust with an MRN77 mass distribution (Fig. 16, *right panel*), it becomes apparent that the coagulation process has enabled the disk to become rather transparent. The overall disk features are in general similar to those resulting from the simple spherical grain model.

The SED shown in Figure 15 (*right panel*) is similar to the SED of model 3MS (*left panel*). The SED generated using the coagulated dust from the 3MS_CCA simulation (*solid line*, *right panel*) displays some differences with respect to the SED using noncoagulated dust: there is a slight shift in the emission peak to shorter wavelengths, lower far-infrared fluxes, enhanced mid-infrared emission, and a less prominent silicate absorption feature.

6. DISCUSSION AND CONCLUSIONS

We have shown that dust coagulation proceeds at an early phase during the formation of a protostellar accretion

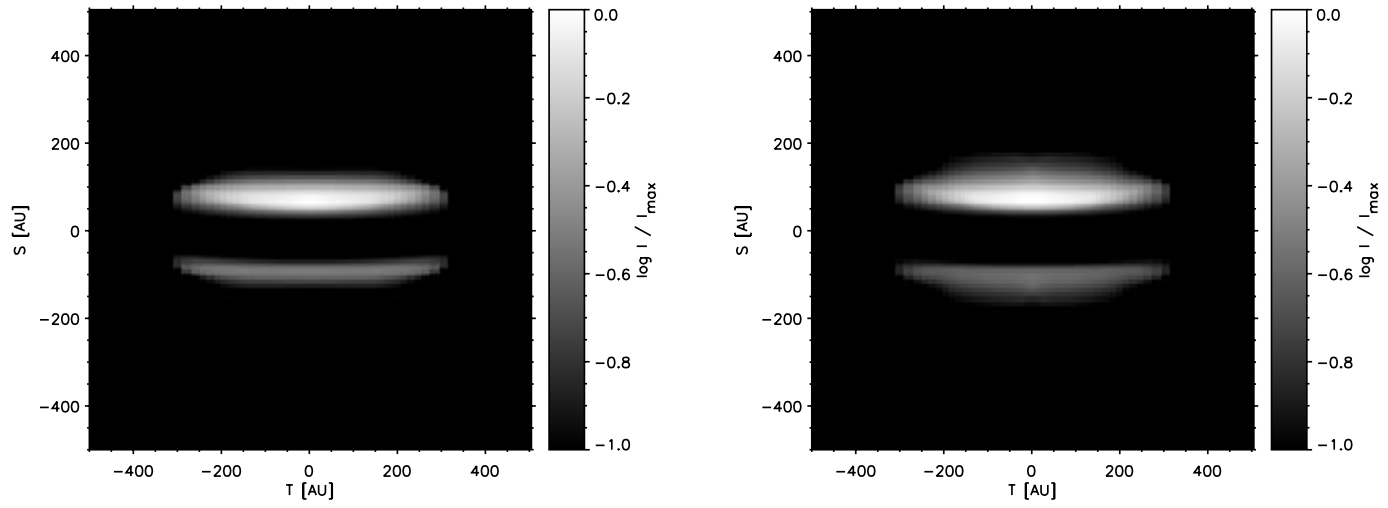

FIG. 14.—Dust continuum emission of model 3MS, 11,400 yr at an angle of inclination of $\theta = 85°$. *Left:* Continuum emission map at $\lambda = 3.6$ μm using coagulated dust as calculated. *Right:* Comparison emission map using unmodified dust.

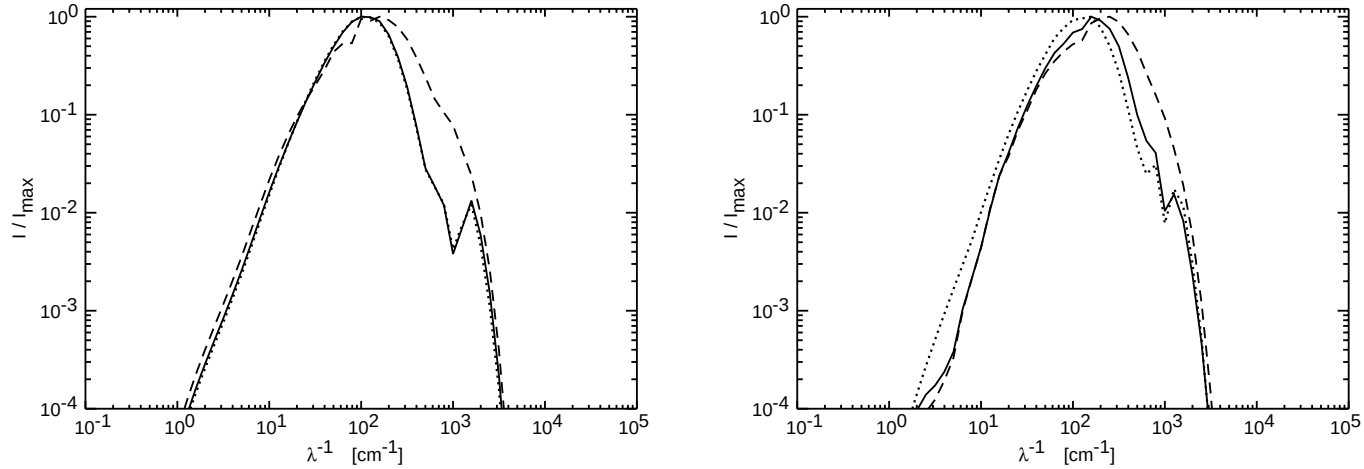

FIG. 15.—Emission spectra resulting from simulations leading to coagulated dust (*solid line*), with unmodified dust (*dotted line*), or assuming monodisperse dust (*dashed line*) with $a = 22$ μm (model 3MS) and $r_{ex} = 0.2$ mm (3MS_CCA). The rotation axis of the disk is inclined at an angle $\theta = 85°$ with respect to the line of sight. *Left:* Model 3MS, 11,400 yr. *Right:* Model 3MS_CCA, 12,600 yr.

disk. Small grains with $a \lesssim 0.1$ μm are removed from the mass spectrum quickly and effectively in the midplane of the accretion disk within $\sim 10^3$ yr. Here large particles with sizes of several times 10 μm can be produced by coagulation. The maximum grain size that can be quickly produced by coagulation during the collapse and initial accretion of material onto the disk depends crucially on the assumed sticking strength of the dust particles. In this respect the process of ice sublimation plays an important role: when the grain surface is coated with material that enhances the grain-to-grain adhesion, the degree of coagulation can be significantly increased.

In the accretion shock front relative velocities of several kilometers per second are achieved as a result of the size-dependent coupling to the gas. Compact spherical grains decouple at higher gas densities (and thus earlier during the evolution) than fractal dust coagulates. Particle shattering of compact spherical grains was not critically important during the evolution of the intermediate-mass protostars considered here. We infer, however, by appropriate scaling of masses and luminosities (see Suttner et al. 1999) that shattering should be important for high-mass protostars. For the high-mass case radiative acceleration will become increasingly more effective in causing a size-dependent spread of dust drift velocities. Assuming BCCA grains that break apart at even relatively small collision energies (as in the model of Dominik & Tielens 1997), particle shattering gains some importance for the lower cloud masses considered here. Within the accretion shock, grains are shattered and the maximum grain size is limited to several times 10 μm. However, the number of very small debris particles thus produced is negligible in the total grain mass spectrum.

Gas-dust drift leads to depletion of dust in the immediate vicinity of the accretion disk everywhere except in the equatorial regions. In particular, the gas-to-dust mass ratio can be lowered by a factor of 2–4 within the accretion shock. Whereas for a cloud clump mass of 1 $M_\odot$ radiative acceleration of dust grains is negligible, for clump masses $\gtrsim 3$ $M_\odot$ radiative acceleration of dust grains becomes increasingly important. Depending on how well the radiation field of the central source is shielded by the disk, the infall of dust particles can be hindered in the polar regions, whereas in

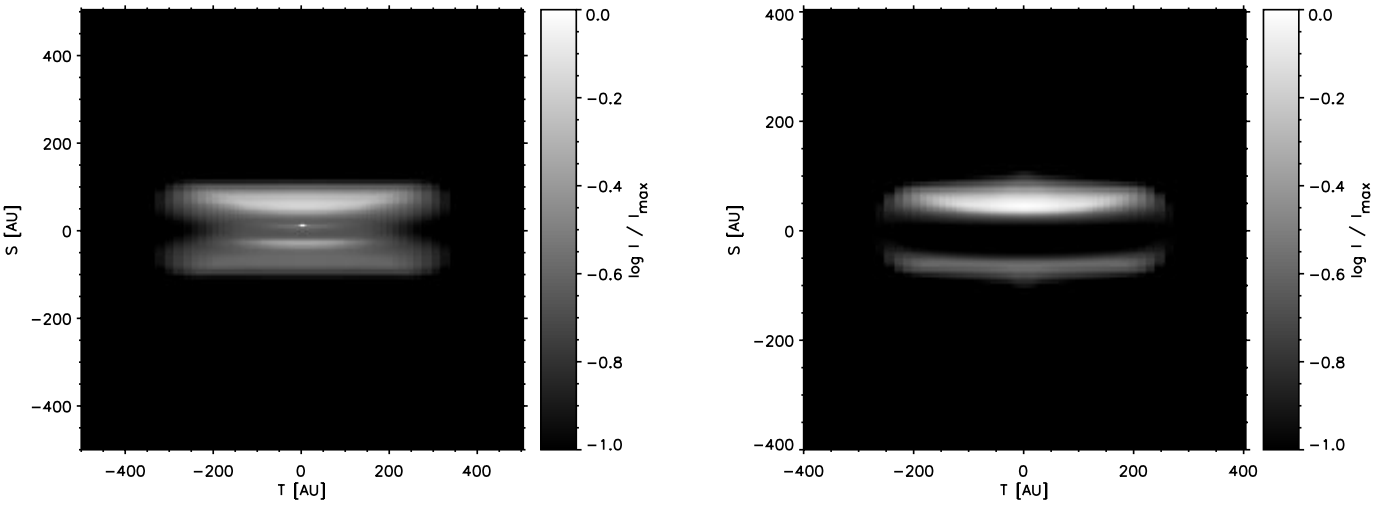

FIG. 16.—Dust emission of model 3MS_CCA, 12,600 yr. The rotation axis is inclined at an angle $\theta = 85°$ with respect to the line of sight. *Left:* Continuum emission map at $\lambda = 3.6$ μm using coagulated dust. *Right:* Emission map assuming unmodified dust.

the equatorial regions the dust moves radially inward faster than the gas.

The optical and physical properties of grains are strongly affected by coagulation. The specific extinction coefficient in the visual to UV can be lowered by more than an order of magnitude in the equatorial plane as a result of coagulation. The grain temperature in the midplane and the grains' capacity for "freezing out" molecules are correspondingly affected. Although the local variations of the optical coefficients are large, the only significant effect to observational properties is a reduction of the near-infrared dust opacity in the wavelength range between 1 and 100 μm, which is most prominent for "robust" BCCA particles. Polarization of starlight should supply an additional appropriate observational tool to determine the degree of coagulation.

The differences of the global characteristics of the simulations using the simple approximation of compact spherical grains, BPCA dust, and BCCA dust are not as dramatic as may have been naively expected. For all three cases the hydrodynamical structure (in particular, gas density and velocity) is strikingly similar. Thus, we feel justified in using our rather crude dust models to perform hydrodynamic simulations of low- and intermediate-mass collapsing clouds and subsequently assume more sophisticated detailed dust models to generate emission maps, polarization maps, and SEDs.

Finally, we note that D'Alessio et al. (1999) find that synthetic 1 μm images of accretion disks around low-mass stars appear to have too large geometrical thicknesses to be consistent with observation, under the assumption that dust is well mixed with the gas. Our study shows that the issue might be resolved by taking into proper account the differential advection of dust grains.

We are grateful to Thomas Henning, Doug Lin, and Rainer Schräpler for helpful discussions and to an anonymous referee for useful suggestions. The research described in this paper was carried out by the Jet Propulsion Laboratory (JPL), California Institute of Technology, and was supported by the "Deutsche Forschungsgemeinschaft" (DFG) under the "Physics of Star Formation" program (grant Yo 5/20-2) and the National Aeronautics and Space Administration (NASA) under grant NRA-99-01-ATP-065. The calculations were performed on workstations at JPL and the "Rechenzentrum der Universität Würzburg," on a Cray T90 at the "HLRZ Jülich," and on an SP2 parallel computer at the same facility.

APPENDIX

Here we give an analytic expression for the kernel $\gamma(m, m', m'', \delta v(m', m''))$ in the shattering equation of § 2.3. As stated in § 3.1, the integral of the shattering equation is discretized by summing over the dust mass space ranging from m_1 to m_N (or, equivalently, from a_1 to a_N). Thus, γ transforms to the discrete function g_{ijk}, from which the debris distribution $G_k(m_i, m_j, \delta v_{ij}) = g_{ijk}\, m_k/(m_i + m_j)$ can be separated.

For $v_{\rm crit} \le \delta v_{i,j} < v_{\rm cat}$ and $wm_j \in [m_k^-, m_k^+]$,

$$G_k(m_i, m_j, \delta v_{ij}) = \frac{m_j}{m_i + m_j}\,(1 - w)\,. \tag{A1}$$

For $v_{\rm crit} \le \delta v_{i,j} < v_{\rm cat}$ and $a_k \le a_{\rm max}$,

$$G_k(m_i, m_j, \delta v_{ij}) = \frac{m_j}{m_i + m_j}\, w f_{\rm MRN}\,. \tag{A2}$$

For $\delta v_{i,j} \ge v_{\rm cat}$ and $a_k \le a_{\rm max}$,

$$G_k(m_i, m_j, \delta v_{ij}) = f_{\rm MRN}\,. \tag{A3}$$

Otherwise, $G_k(m_i, m_j, \delta v_{ij}) = 0$.

We have used the following assumptions and definitions:

$$m_i \ge m_j\,,$$

$$m_k^- = \frac{m_k + m_{k-1}}{2} \qquad (m_k^+ = m_{k+1}^-)\,,$$

$$w = \left(\frac{\delta v_{ij}}{3.64\ {\rm km\ s^{-1}}}\right)^{16/9}\,,$$

$$v_{\rm crit} = 2.7\ {\rm km\ s^{-1}}\,,$$

$$v_{\rm cat} = \max\left[v_{\rm crit},\ 1.13\ {\rm km\ s^{-1}}\left(\frac{m_i}{m_j}\right)^{9/16}\right],$$

$$a_{\rm max} = \begin{cases} 0.28\left(\dfrac{wm_j}{\varrho_{\rm bulk}}\right)^{1/3} & \text{if } \delta v_{ij} < v_{\rm cat}\,, \\ 0.20\,\dfrac{a_i\, v_{\rm cat}}{\delta v_{ij}} & \text{if } \delta v_{ij} \ge v_{\rm cat}\,. \end{cases}$$

The formulae were adapted from the work of Jones et al. (1996). Here w denotes the ejected crater mass in units of the projectile mass, $v_{\rm cat}$ the critical velocity for the onset of total disruption of the target, and $a_{\rm max}$ the radius of the largest debris particle. The debris particles are redistributed according to an MRN77 size distribution $f_{\rm MRN77}$ between $a_{\rm min} = a_1$ and $a_{\rm max}$ (i.e., between $m_{\rm min} = m_1$ and $m_{\rm max}$):

$$f_{\rm MRN77} = \frac{m_k^{-5/6}\,\Delta m_k}{\sum_{i=1}^{\rm max} m_i^{-5/6}\,\Delta m_i}\,. \tag{A4}$$

REFERENCES

Beckwith, S. V. W., Henning, T., & Nakagawa, Y. 2000, in Protostars and Planets IV, ed. V. Mannings, A. P. Boss, & S. S. Russell (Tucson: Univ. Arizona Press), 533
Black, D. C., & Bodenheimer, P. 1975, ApJ, 199, 619
Bridges, F. G., Supulver, K. D., Lin, D. N. C., Knight, R., & Zafra, M. 1996, Icarus, 123, 422
Chokshi, A., Tielens, A. G. G. M., & Hollenbach, D. 1993, ApJ, 407, 806
D'Alessio, Calvet, N., Hartmann, L., Lizano, S., & Cantó, J. 1999, ApJ, 527, 893
Dominik, C., & Tielens, A. G. G. M. 1997, ApJ, 480, 647
Douglas, J., & Rachford, H. H. 1956, Trans. Am. Math. Soc., 82, 421
Draine, B. T., & Lee, H. M. 1984, ApJ, 285, 89
Epstein, P. 1923, Phys. Rev., 22, 710
Fischer, O., Henning, Th., & Yorke, H. W. 1994, A&A, 284, 187
Henning, Th., & Stognienko, R. 1996, A&A, 311, 291
Jones, A. P., Tielens, A. G. G. M., & Hollenbach, D. 1996, ApJ, 469, 740
Lang, K. R. 1974, Astrophysical Formulae: A Compendium for the Physicist and Astrophysicist (Berlin: Springer)
Levermore, C. D., & Pomraning, G. C. 1981, ApJ, 248, 321
Mathis, J. S., Rumpl, W., & Nordsieck, K. H. 1977, ApJ, 217, 425 (MRN77)
Mizuno, H. 1989, Icarus, 80, 189
Mizuno, H., Markiewicz, W. J., & Völk, H. J. 1988, A&A, 195, 183
Ossenkopf, V. 1993, A&A, 280, 617
Poppe, T., & Blum, J. 1997, Adv. Space Res., 20, 1595
Schmitt, W., Henning, Th., & Mucha, R. 1997, A&A, 325, 569
Shakura, N. I., & Sunyaev, R. A. 1973, A&A, 24, 337
Sonnhalter, C., Preibisch, Th., & Yorke, H. W. 1995, A&A, 299, 545
Supulver, K. D., Bridges, F. G., Tiscareno, S., & Lievore, J. 1997, Icarus, 129, 539
Suttner, G., Yorke, H. W., & Lin, D. N. C. 1999, ApJ, 524, 857
Tassoul, J.-L. 1978, Theory of Rotating Stars (Princeton: Princeton Univ. Press)
Völk, H. J., Jones, F. C., Morfill, G. E., & Röser, S. 1980, A&A, 85, 316
Vrba, F. J., Coyne, G. V., & Tapia, S. 1993, AJ, 105, 1010
Weidenschilling, S. J. 1977, MNRAS, 180, 57
———. 1984, Icarus, 60, 553
Weidenschilling, S. J., & Cuzzi, J. N. 1993, in Protostars and Planets III (Tuscon: Univ. Arizona Press), 1031–1060
Weidenschilling, S. J., & Ruzmaikina, T. V. 1994, ApJ, 430, 713
Wetherill, G. W. 1990, Icarus, 88, 336
Wurm, G. 1997, Ph.D. thesis, Univ. Jena
Yorke, H. W. 1979, A&A, 80, 308
———. 1988, in Radiation in Moving Gaseous Media: 18th Saas-Fee Adv. Course (Geneva: Geneva Obs.), 210–224
Yorke, H. W., & Bodenheimer, P. 1999, ApJ, 525, 330
Yorke, H. W., Bodenheimer, P., & Laughlin, G. 1995, ApJ, 443, 199
Yorke, H. W., & Henning, T. 1994, in IAU Colloq. 146, Molecules in the Stellar Environment, ed. U. G. Jorgensen (Berlin: Springer), 186
Yorke, H. W., & Kaisig, M. 1995, Comput. Phys. Commun., 89, 29